A&A, 687, A191 (2024)
https://doi.org/10.1051/0004-6361/202449546

Astronomy & Astrophysics

Observed seasonal changes in Martian hydrogen chloride explained by heterogeneous chemistry⋆

Benjamin M. Taysum[1,2], Paul I. Palmer[1,2], Kevin Olsen[3], Mikhail Luginin[4], Nikolay Ignatiev[4], Alexander Trokhimovskiy[4], Alexey Shakun[4], Alexey V. Grigoriev[5], Franck Montmessin[6], and Oleg Korablev[4]

[1] School of GeoSciences, University of Edinburgh, Edinburgh, UK
e-mail: benjamin.taysum@dlr.de
[2] Centre for Exoplanet Science, University of Edinburgh, Edinburgh, UK
e-mail: pip@ed.ac.uk
[3] Department of Physics, University of Oxford, Oxford, UK
[4] Space Research Institute (IKI), Moscow, Russia
[5] Research School of Astronomy and Astrophysics, Australian National University, Canberra, ACT 2611, Australia
[6] LATMOS/IPSL, UVSQ Université Paris-Saclay, Sorbonne Université, CNRS, Guyancourt, France

Received 8 February 2024 / Accepted 3 May 2024

ABSTRACT

Aims. The aim of this work is to show that the seasonal changes and vertical distribution profiles of hydrogen chloride (HCl) on Mars, as observed by the ExoMars Trace Gas Orbiter, are consistent with the production of gas-phase chlorine atoms from airborne dust and a subsequent rapid uptake of HCl onto water ice particles.
Methods. A 1D photochemistry model was equipped with a chlorine reaction network and driven by dust, water ice, and water vapour profiles measured by the ExoMars Trace Gas Orbiter instrumentation in Mars year 34. The release of Cl and O atoms from airborne dust via the hydration and photolysis of perchlorate within dust grains was parameterised using prior laboratory studies, and the heterogeneous uptake of chlorine species onto dust and water ice was included for processes known to occur in Earth's atmosphere.
Results. Observed seasonal variations in Martian HCl are reproduced by the model, which yielded low HCl abundances (<1 ppbv) prior to the dust season that rise to 2–6 ppbv in southern latitudes during the dust season. Structured atmospheric layers that coincide with locations where water ice is absent are also produced. As a consequence of the Cl atoms released via our proposed mechanism, the atmospheric lifetime of methane is shortened by two orders of magnitude. This suggests that the production of Cl induced by the breakdown of hydrated perchlorate via UV radiation (or another electromagnetic radiation) in airborne Martian dust, consistent with observed profiles of HCl, could help reconcile reported variations in methane with photochemical models.

Key words. planets and satellites: atmospheres – planets and satellites: terrestrial planets

1. Introduction

The detection of hydrogen chloride (HCl) in the Martian atmosphere during the Mars year (MY) 34 global dust storm (Korablev et al. 2021; Olsen et al. 2021) marked the first detection of an atmospheric halogenated gas on the planet. These observations collected by the Atmospheric Chemistry Suite (ACS; Korablev et al. 2018) aboard the ExoMars Trace Gas Orbiter (TGO; Vago et al. 2015) were later corroborated by the Nadir and Occultation for Mars Discovery (NOMAD) spectrometer (Aoki et al. 2021), another TGO instrument. Prior astronomical searches for gas-phase chlorine species only resulted in upper limits for HCl at various points throughout Mars's orbit. The Goddard Space Flight Center (GSFC) postdisperser and the Kitt Peak National Observatory's Fourier transform spectrometer were able to infer a 2σ HCl upper limit of <2 ppbv during the dusty season at a solar longitude (L_S) of 222° (Krasnopolsky et al. 1997). Measurements of sub-millimetre wavelengths collected by the *Herschel* Space Observatory from its Earth orbit allowed an upper limit of 200 pptv to be determined at 77° L_S (Hartogh et al. 2010), suggesting that the chlorine chemistry on Mars is not particularly important, if it exists. Villanueva et al. (2013) used data collected by ground-based instruments over a 4-yr observing period to search for HCl and methyl chloride (CH_3Cl), a product of chemical reactions between methane and non-methane volatile organic compounds. Villanueva et al. (2013) inferred upper limits of <0.6 ppbv for HCl and <14.3 ppbv for CH_3Cl at 12° L_S, and 1.5 ppbv and 2.1 ppbv of HCl at 324° L_S and 352° L_S, respectively. It was only the recent observational campaign by the ExoMars TGO (Korablev et al. 2021; Olsen et al. 2021; Aoki et al. 2021) that helped piece together the seasonal chlorine cycle that is currently active on Mars, emphasising the importance of the advancements in measurement technology that made the HCl detections by ACS and NOMAD possible.

The TGO project selected HCl as one of its target compounds because of its association with volcanic outgassing processes (Zurek et al. 2011; Timmreck 2012). Here, we discuss whether

⋆ 1D model files used to produce the results of this paper can be found on the Zenodo data repository at https://zenodo.org/records/10955516. Aerosol profiles used in this paper, retrieved by the ACS TIRVIM-NIR spectrometer channels, can be found on the Mendeley Data repository at http://dx.doi.org/10.17632/9yrrw4t9gw.1, and are published here for the first time.

volcanic emissions could help explain the seasonal production of Mars's atmospheric HCl. On Earth, rates of volcanic emissions of sulfur compounds and methane (von Glasow 2010) are 20–50 times higher than emissions of HCl (Ohno et al. 2013). There is little evidence of volcanic emissions on Mars. Ground-based spectroscopy measurements suggest an upper limit of <1 ppbv for Martian sulfur dioxide (SO_2; Krasnopolsky 2005). Analysis of ground-based measurements of sub-millimetre wavelengths relevant to carbonyl sulfide (OCS) and SO_2 over regions of distant past Martian volcanic activity (Hiesinger & Head III 2004) resulted in estimated upper limits of 1.8 ppbv and 3.1 ppbv, respectively (Khayat et al. 2017). More recently, in MY 34–35, ACS failed to detect the sulfur species SO_2, H_2S, or OCS (Braude et al. 2022). Furthermore, analysis of Martian seismic activity, closely linked with volcanic activity, from the first ten months of data collection by the NASA InSight lander (Banerdt et al. 2020) shows that Mars's seismic noise is roughly 500 times lower than on Earth (Lognonné et al. 2020). The lack of significant seismic activity and the absence of sulfur-containing atmospheric species associated with volcanic outgassing strongly suggests that volcanism is not the source of the atmospheric HCl observed by the ACS and NOMAD.

Using the ACS mid-infrared (MIR) channel, Korablev et al. (2021) found atmospheric HCl values of 1–4 ppbv during the MY 34 global dust storm, some 20 times higher than expected based on previously inferred upper limits (Hartogh et al. 2010; Villanueva et al. 2013). ACS/MIR data from MY 35 supported the idea that anomalously large HCl values were linked with the start of the dust season ($L_S \simeq 180°$). NOMAD data collected in MY 34–35 (Aoki et al. 2021) corroborated this finding, and showed that a global dust storm event is not necessary to explain anomalous HCl values. This unexplained appearance of anomalously large HCl levels combined with the rapid decline in atmospheric HCl after the dust season ($L_S \simeq 320°$) suggests a sink stronger than that produced by gas-phase photochemistry alone. Aoki et al. (2021) note that the disappearance of HCl at $L_S \simeq 320°$ occurs simultaneously with an annually repeating regional dust storm, suggesting a role for dust in the transient appearance and disappearance of HCl.

Based on our current understanding of Martian atmospheric chemistry, the photochemical lifetime of HCl varies between >90 and >1000 sols depending on the season and latitude (Aoki et al. 2021). However, a lifetime shorter than 75 sols is required to explain the changes in HCl in MY 34–35 observed by ExoMars TGO instruments. To reconcile photochemical models with TGO measurements of HCl, we need a production term that is related to the presence of dust and a loss term that can explain the faster-than-expected decrease in HCl at the end of the dust season. Krasnopolsky (2022) used a 1D chemistry model to study the release of HCl and ClO from heterogeneous reactions between dust and H and O atoms. Their model was able to generate HCl at the ppbv levels observed by ExoMars TGO instruments during dust storm conditions and non-detectable levels in environmental conditions corresponding to the aphelion. Observed HCl profiles show vertical structures that vary with latitude and solar longitude and correlate with the vertical structure of atmospheric water vapour (H_2O; Aoki et al. 2021). However, Krasnopolsky (2022) did not compare their model with observations. They did show that including a small heterogeneous uptake of HCl on water ice and mineral dust was capable of lowering the HCl lifetime to shorter than 75 sols, the value required to explain the disappearance of HCl at the end of the dust season.

The photolysis of HCl produces chlorine atoms (Cl) that can subsequently influence the atmospheric chemistry ofoxygen and hydrogen oxides on Mars. These Cl atoms are also an efficient sink for atmospheric methane (CH_4) on Earth (Hossaini et al. 2016), and as we discuss below they could influence Martian methane chemistry. Atmospheric methane has been reported by the Planetary Fourier Spectrometer on the Mars Express satellite (Formisano et al. 2004; Geminale et al. 2008, 2011) and ground-based telescopes (Krasnopolsky et al. 2004; Mumma et al. 2009), and in situ by the Curiosity Rover (Webster et al. 2015, 2021). However, no detections of atmospheric methane have been reported by the ExoMars TGO (Korablev et al. 2019; Knutsen et al. 2021). The latest revised upper limit of atmospheric methane is 20 pptv (Montmessin et al. 2021). Multiple ground-based observations have similarly failed to detect methane on Mars (Encrenaz et al. 2006; Krasnopolsky 2012; Villanueva et al. 2013; Aoki et al. 2018).

The reported transient detections of atmospheric methane have also been questioned because they require an atmospheric loss process that is some 600 times quicker than anything currently included in Martian photochemical models (Lefèvre & Forget 2009; Wong et al. 2003; Summers et al. 2002; Taysum & Palmer 2020). Such a loss process would also be inconsistent with what we currently know about the Martian atmospheric redox budget (Zahnle et al. 2011). However, the recent observations of HCl by the ExoMars TGO instrumentation (Korablev et al. 2021; Olsen et al. 2021; Aoki et al. 2021) could lead one to infer that the presence of Cl atoms indicates a significant and rapid loss of atmospheric methane.

In this study, we explored the gas-phase and heterogeneous chemistry of HCl and compared our 1D photochemical model with ACS and NOMAD data collected in MY 34. In Sect. 2, we describe our 1D photochemical model and our assumptions. In Sect. 3, we evaluate our model HCl calculations with ACS and NOMAD retrievals. In Sect. 4, we discuss our results in the context of previous research and model limitations. We conclude the paper in Sect. 5.

2. Model of Martian atmospheric photochemistry

We used a 1D model of Martian atmospheric photochemistry to interpret satellite observations of Martian chlorine chemistry. In this section, we provide a summary of the underlying photochemistry model, described in detail by Taysum & Palmer (2020), and outline the additional model development needed to understand Martian chlorine chemistry.

2.1. Baseline photochemical model

The model framework is based on the 1D photochemistry submodule of the LMD-UK version of the 3D Mars general circulation model (Forget et al. 1999; Lefèvre et al. 2004; Holmes et al. 2019). We used a dynamical timestep of ≃1800 s (48 steps per Mars sol) across 25 vertical levels that range from the surface to approximately 70 km. At altitudes lower than 2 km, the model levels are separated by <0.5 km to help the model describe turbulent diffusion processes close to the surface. Between 2 and 20 km the vertical resolution progressively coarsens to $\Delta z \simeq 10$ km. Above 20 km, the vertical resolution remains approximately 10 km. The discretised photochemistry equations are evaluated using a chemistry sub-timestep of ≃600 s to decrease the stiffness of the model photochemical reactions. The classical diffusion equation developed by Mellor & Yamada (1982) was used to calculate vertical diffusion between our model layers, which is described by Forget et al. (1999).

To improve the accuracy of the 1D model photochemical calculations, we used time-dependent meteorological boundary conditions of physical atmospheric parameters from the Mars Climate Database v6.1 (MCDv6.1; Millour et al. 2015). The model interpolates vertical profiles of temperature, pressure, and wind with respect to planetary latitude and longitude, solar longitude, local time, and altitude above the surface. Similarly, we interpolated profiles of long-lived (lifetimes exceeding one Mars year) inorganic trace gas species CO_2, CO, H_2, H_2O, and O_2.

To study individual ACS/MIR observations, we drove the model using both the standard climatological and the MY34 climatology MCDv6.1 datasets. We used optical opacities extracted from the MCDv6.1 standard climatology and MY34 climatology datasets, an assimilation of opacity measurements made by the Mars Climate Sounder (Montabone et al. 2020). We chose to focus our 1D model study on MY34 because it is the year in which Korablev et al. (2021) detected atmospheric HCl with the ACS/MIR instrument.

The model includes 14 inorganic gas-phase gases and 12 organic gas-phase species governing the oxidation of methane (Taysum & Palmer 2020), and 13 chlorine-containing gas-phase species. The model also includes heterogeneous chemistry routines involving water ice and dust aerosols. Here, we provide a comprehensive description of the chemical reactions used in this study. Table C.1 lists all of the tracers used in the 1D photochemical model. For details about the methane oxidation scheme and the model physics such as the vertical diffusion routines we refer the reader to Taysum & Palmer (2020) and Forget et al. (1999), respectively.

2.2. Heterogeneous chlorine chemistry

The main photochemical sinks of HCl on Mars include gas-phase reactions with OH, $O(^3P)$, and photolysis (cl_{14}, cl_{40} from Table D.3 and j_{HCl} from Table D.1). They result in a photochemical lifetime longer than the 75 sols required to explain falling HCl abundances after the dust season ends (Aoki et al. 2021; Olsen et al. 2021). This suggests that heterogeneous chemistry needs to be invoked to reconcile photochemical models that describe atmospheric HCl and observations.

A recent study using ACS/MIR data measured the ratio of the $H^{35}Cl$ and $H^{37}Cl$ isotopologues for 29 HCl detections through MY 34–35 (Trokhimovskiy et al. 2021). They report a mean $\delta^{37}Cl$ value of $-7 \pm 20‰$, which lies within the range of –3.8–8.6 ‰ inferred from the analysis of 16 Martian meteorite samples (Sharp et al. 2016). The Sample Analysis at Mars (SAM) instrument aboard the Curiosity Rover reported a value of -7 ± 44 ‰ for the $\delta^{37}Cl$ content of HCl, determined by heating a sand sample collected from the Rocknest sand deposit (Farley et al. 2016). While the associated measurement uncertainties are large, this is the only sample we have for modern-day dust that has been lofted to the atmosphere by aeolian processes. The similarities in Cl isotopologue fractionation in the gas-phase and solid-state on Mars suggest that Martian atmospheric chlorine originates from dust-atmosphere interactions. Perchlorate (ClO_4^-) has been detected in Martian soils at approximately 0.5 wt% by the Phoenix lander (Hecht et al. 2009; Kounaves et al. 2014), and chlorine-containing minerals are regularly detected by other in situ instruments such as the two Viking landers (Clark et al. 1982), the Pathfinder lander (Economou 2001), the Spirit Rover (Gellert et al. 2004), and the Opportunity Rover (Rieder et al. 2004). A global map of the Cl content of the Martian top soil, retrieved by the Mars Odyssey Gamma Ray Spectrometer (Keller et al. 2006), determined a mean weight percentage of 0.49%. These data showed chlorine concentrations ranging between 0.25 and 1.04% at Central Elysium Planitia (approximately 3°N, 154.7°E; Diez et al. 2009).

Collectively, these findings, in context with the profiles of HCl retrieved by the ACS and NOMAD instruments being correlated with the Martian dust cycle and changes in H_2O vapour profiles (Korablev et al. 2021; Olsen et al. 2021; Aoki et al. 2021), point to chlorine-containing dust grains playing a role in Mars's atmospheric chlorine cycle. In this study, we propose a mechanism that describes the heterogeneous loss of HCl on dust and ice surfaces and explore three possible mechanisms that describe three production of HCl on Mars. We present below the HCl production mechanism from UV-irradiated and hydrated airborne dust because the resulting HCl profiles agree best with TGO data; the other two mechanisms are described in Appendix A.

2.2.1. Heterogeneous loss of chlorine

We assessed heterogeneous chemical reactions that occur between gas-phase chlorine compounds and mineral dust and ice crystals in the atmosphere of Earth. This approach has previously been used to model the uptake of OH and HO_2 radicals on water ice in Mars photochemical models (Lefèvre et al. 2008). More recently, Daerden et al. (2023) presented a detailed study of the difficulties of simulating heterogeneous chemistry on Mars. They show that the HO_2 uptake onto ice used by current models may be over estimated, while gas-phase interactions with dust could be complicated by possible chemical ageing of the dust grain – a process whereby the chemical characteristics of the dust particle surfaces have been altered by long-term exposure to gas-phase uptake, UV photolysis, and high energy particles.

The uptake of HCl onto mineral dust is an effective loss process for chlorine on Earth (Sullivan et al. 2007). The uptake of HCl with $CaCO_3$ in our model is motivated by the mechanism proposed by Kelly & Wexler (2005). We describe the uptake of HCl onto $CaCO_3$ in the dust as

$$2HCl_{(g)} + CaCO_{3(s)} \longrightarrow CaCl_{2(s)} + H_2O_{(g)} + CO_{2(g)}, \quad (1)$$

for which we find the associated enthalpy change is –39.63 kJ mol^{-1}. The Phoenix Lander reported a weight percentage of 3–5% of $CaCO_3$ in the Martian soil (Boynton et al. 2009), which further supports our use of this heterogeneous loss mechanism in our Mars photochemical model. We adopt edan uptake coefficient with a negative temperature dependence based on a fit to empirical data (Huynh & McNeill 2020, 2021) at pressures and temperatures relevant to Earth's stratosphere (T = 207 K and 296 K at P = 760 Torr). The fit adopts the form of the mediated precursor model (MPM; Berland et al. 1997). Derived for gas particle uptake onto water ice particles, the MPM requires clean uptake sites on the particle surface; it does not account for the burial of molecules onto surface sites. We acknowledge that the pressures assumed by this model are approximately 100 times larger than those experienced at Mars's surface ($P \simeq 7.5$ Torr), which may result in model error. Daerden et al. (2023) also find that uptake coefficients on terrestrial mineral dust for the uptake of HO_2 and H_2O_2 produce changes to their model O_3 and H_2O_2 columns that are too large. They postulate that the reactivity of Martian dust may be lower than Earth's due to enhanced chemical ageing. To approximate the lower efficiency of the reactions due to this ageing, and the decreases in uptake efficiency expected for imperfect dust particle grains under atmospheric conditions, we scaled the reaction rate by a factor of 10^{-1}. This factor is highly uncertain due to the lack of constraints from

laboratory experimentation, and should be a focus of future work.

Uptake of HCl also occurs on water ice crystals in Earth's atmosphere (Abbatt et al. 1992; Isakson & Sitz 1999) for which reaction rates have been measured (Hynes et al. 2001) and used in Earth atmosphere models. The uptake coefficient (γ) of a heterogeneous reactions is the fraction of successful chlorine release reactions for every H_2O molecule making contact with the dust surface. There is consensus that the uptake rate is fast at stratospheric temperatures ($\gamma \simeq 0.1$) and should follow a negative temperature dependence (Burkholder et al. 2019). However, there is less agreement on the exact numerical value of the uptake coefficient and the chemical or physical nature of the reaction (Leu 1988; Hanson & Ravishankara 1992; Rieley et al. 1995; Hynes et al. 2002, 2001). We used the negative temperature dependent coefficient derived by Hynes et al. (2001) that takes the form of the MPM (Berland et al. 1997). We then calculated the surface coverage, θ_{Lang}, of the ice particles using the Langmuir adsorption method for a non-dissociative reaction:

$$\theta_{\mathrm{Lang}} = \frac{K_{\mathrm{Lang}} N_{\mathrm{HCl}}}{1 + K_{\mathrm{Lang}} N_{\mathrm{HCl}}}, \tag{2}$$

with a temperature independent equilibrium constant K_{Lang} of 9.6E-11 $\mathrm{cm^3\ mol^{-1}}$ (Kippenberger et al. 2019), and HCl number density N_{HCl} (mol $\mathrm{cm^{-3}}$). The reaction rate for HCl uptake on ice was then multiplied by the factor $(1 - \theta_{\mathrm{Lang}})$. To account for imperfections in the ice crystals, we applied a factor of 10^{-1} to account for an expected decrease in uptake efficiency, consistent with our method for dust uptake. Values for the uptake coefficients were calculated across the temperature range of 205–230 K at pressures of 1.7–2.0 Torr. This pressure and temperature range is typically experienced on Mars between altitudes of 10–20 km. The HCl partial pressures used in the experiments were $0.4–2.0\times10^{-6}$ Torr ($0.5–2.6\times10^{-4}$ Pa), roughly 2–3 orders of magnitude larger than observed on Mars. These larger partial pressures in the laboratory chamber could potentially produce errors in the uptake coefficients when applied to the Martian atmosphere. Upon adsorption to the ice surface, HCl is capable of photolysing and reintroducing Cl and H atoms into the atmosphere. However, when the ice crystal is growing, HCl molecules can become trapped beneath the ice crystal surface (Kippenberger et al. 2019). In daytime conditions, we model the uptake reaction as

$$\mathrm{HCl + Ice \longrightarrow H + Cl.} \tag{3}$$

During nighttime conditions, we did not track the products and we assumed the HCl molecule is terminally lost.

We included the heterogeneous loss of Cl_2 on Martian dust grains using the uptake coefficient of $\gamma = 10^{-3}$ (Burkholder et al. 2019) for the uptake on NaCl, multiplied by the 10^{-2} to represent the magnitude of the weight percentage of solid-state chlorine typically observed in the Martian soil. The final heterogeneous loss of atmospheric chlorine in the 1D model is the uptake of ClO onto water ice, using an uptake coefficient of $\gamma = 10^{-4}$, the upper limit reported by Burkholder et al. (2019). Table D.2 lists the uptake reactions and uptake coefficients used in this study.

The reaction rate coefficients for these heterogeneous reactions, k_{h} ($\mathrm{s^{-1}}$), involving mineral dust and ice crystals take the general form:

$$k_{\mathrm{h}}(T) = \frac{1}{4} \times \upsilon_{\mathrm{X}}(T) \times S \times \gamma_{\mathrm{X}}(T) \times \alpha, \tag{4}$$

where υ_{X} is the thermal velocity of gas-phase species X ($\mathrm{cm\ s^{-1}}$), S denotes the surface area of aerosol per unit volume of air ($\mathrm{cm^2\ cm^{-3}}$), and γ_{X} denotes the dimensionless uptake coefficient of species X on the aerosol. Reactions involving dust are scaled by a factor α representative of the weight percentage of solid-state species considered in the reaction.

We also included reactions that describe the atmospheric chemistry of perchloric acid ($HClO_4$; Table D.3, reactions Cl_{44}–Cl_{51}) following Catling et al. (2010) and Wilson et al. (2016), who argued that the resulting deposition of gas-phase $HClO_4$ to the surface or adsorption to dust-grains may be one of several means of recovering the solid-state perchlorate. We introduced deposition velocities at the surface for HCl and $HClO_4$ of 0.2 $\mathrm{cm\ s^{-1}}$, and 0.5 $\mathrm{cm\ s^{-1}}$ for HOCl, taken from the modelling study of Catling et al. (2010).

Figure 1a shows the partial-column integrated photochemical lifetime of HCl across latitude and solar longitude in the 1D model with and without the heterogeneous chlorine uptake reactions, described above. The partial column is located within the altitude range of 5–35 km, corresponding to the altitude region of TGO's HCl observations. These lifetimes are calculated by fixing the model with a 1 ppbv vertically homogeneous HCl abundance, and driving the model with standard climatological aerosol and H_2O abundances from the MCDv6.1 at longitude 0° E. The total mean column loss of HCl ($\mathrm{mol\ cm^{-2}\ s^{-1}}$) is calculated within the 5–35 km altitude range. The mean density of HCl within this altitude range ($\mathrm{mol\ cm^{-2}}$) is divided by the mean column loss to produce the partial column integrated lifetimes shown in Fig. 1a. Without heterogeneous uptake, HCl lifetimes exceed the 75 sol limit required to explain the rapid disappearance of atmospheric HCl at the end of the dust season (Korablev et al. 2021; Olsen et al. 2021). When we invoke the HCl uptake onto ice and dust, using uptake coefficients derived from laboratory experiments, the HCl lifetimes drop to 1–2 days at high polar (>|45|°) latitudes during winter months, due to uptake on ice crystals and $CaCO_3$ in the dust. At lower latitudes, the HCl lifetimes are reduced to 1–24 h throughout the Martian year due to uptake on water ice and dust.

Figures 1b, c show the individual loss rates of reactions at 71° and 251° L_{S}, corresponding to Mars positioned at orbital aphelion and perihelion, respectively, at latitude 45° N and longitude 0° E. The dominant non-heterogeneous sinks for HCl are the OH radical and UV photolysis. Where ice and dust are present, the heterogeneous uptake of HCl is more than three orders of magnitude more efficient at removing atmospheric HCl than gas-phase photochemistry. Dust is ubiquitous in the atmosphere, with variations in abundances and shapes driven by seasonal changes in wind fields. Water ice is significantly more spatially and temporally variable, but where it does appear the mass loading contents of dust and ice are comparable (Luginin et al. 2020). Below 190 K, the HCl uptake on ice is 2–5 times larger than that on $CaCO_3$ (Table D.2). Uptake onto dust is responsible for lowering the HCl lifetime to 1–10 days across altitudes below the top of dust layers throughout the Martian year, but at the locations of water ice clouds the HCl lifetimes plummet to values of 1–24 h. As we show in Sect. 3.4, the layered structure of water ice clouds is key to driving the layered structures of HCl that are observed by TGO instrumentation between 5 and 35 km (Korablev et al. 2021; Olsen et al. 2021; Aoki et al. 2021). Below 5 km, dust abundances are highest, and polar water ice levels in winter can become large enough to cause the near-surface lifetimes to reduce to 0.5–1 h. Our model approximates the saturation of aerosol surface uptakes so our estimate should be considered conservative.

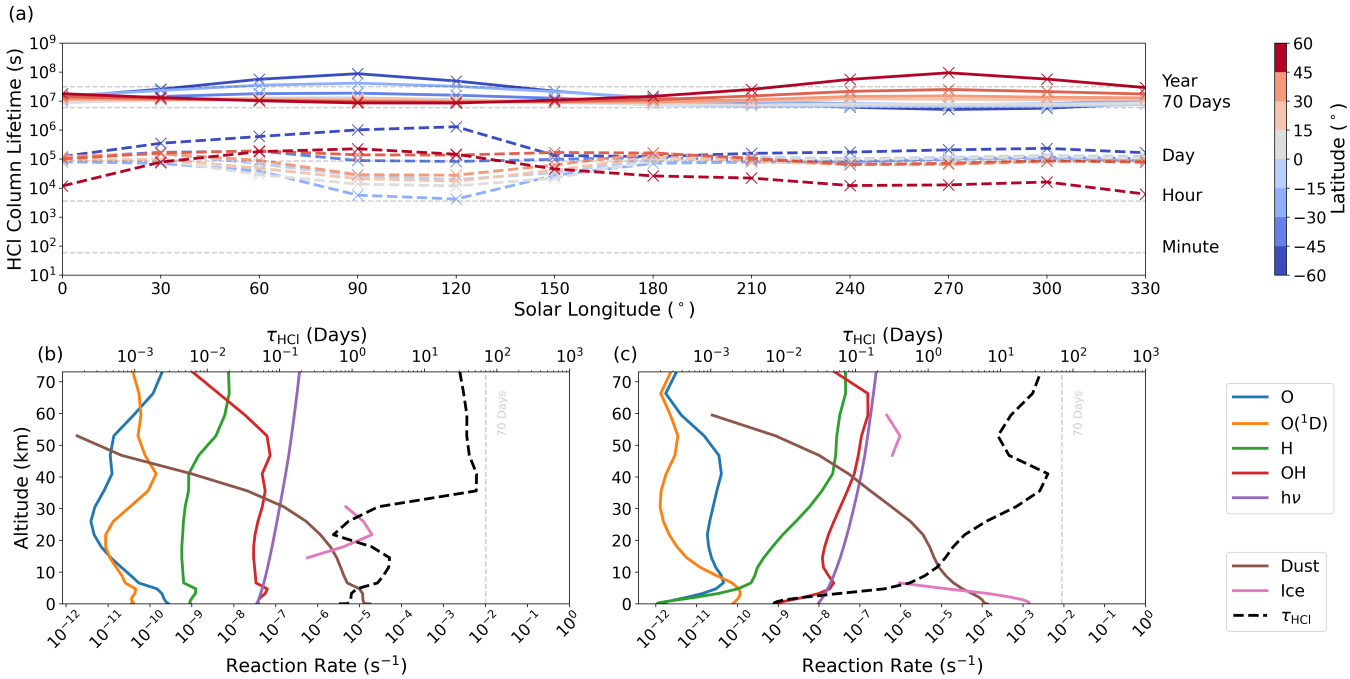

Fig. 1. Photochemical lifetimes of HCl on Mars calculated by the 1-D photochemistry model. (a) The photochemical partial column lifetime (within 5–35 km) of atmospheric HCl without (solid) and with (dashed) the heterogeneous uptake of HCl onto $CaCO_3$ in airborne dust and water ice crystals, photochemical loss rates (s^{-1}) and subsequent photochemical lifetime (τ) of HCl at 45° N at (b) 71° L_S and (c) 251° L_S.

2.2.2. Heterogeneous production of chlorine

Zhang et al. (2021) find that $Mg(ClO_4)_2{\cdot}6H_2O$ in the presence of UV radiation could accelerate the oxidation of methane in an experimental chamber at 300 K and 100 Torr by orders of magnitude. They extrapolated their findings to suggest that the reactions involved could be capable of reducing the lifetime of methane to a range of hours to days at the Martian surface, orders of magnitude shorter than the expected values of centuries, inferred from photochemical models (Taysum & Palmer 2020; Wong & Atreya 2004). However, the reported laboratory results are unclear about whether this increase in methane reactivity is due to reactions on the solid surface or due to the production of Cl atoms and subsequent reaction with methane.

Perchlorate has been reported by multiple in situ instruments (Hecht et al. 2009; Kounaves et al. 2010, 2014; Navarro-González et al. 2010; Fisher et al. 2008). It is known to be hydrophilic, leading scientists to observe that the adsorption of gaseous H_2O can lead to the production of aqueous brine solutions. These condensed solutions can become stable at Martian surface pressures and temperatures (Gough et al. 2011; Primm et al. 2018) and lead to the production of slope lineae features seen by orbiters (Chevrier & Rivera-Valentin 2012; McEwen et al. 2014).

Studies of anhydrous $Mg(ClO_4)_2$ found a significant growth in their sample masses when exposed to environments with relative humidities of <1% due to the uptake of H_2O and conversion to $Mg(ClO_4)_2{\cdot}6H_2O$ (Jia et al. 2018). Other experiments found an approximately linear relationship between the relative humidity and the mass hygroscopic growth factors of $Mg(ClO_4)_2{\cdot}6H_2O$ samples at 278 K after breaching the deliquescence relative humidity of ≃40–50% up to 80% (Gu et al. 2017). Based on these empirical studies, we adopted a linear dependence on relative humidity for the reaction mechanism we describe below.

The mechanism we developed is based on the assumption that perchlorate, once hydrated by atmospheric H_2O, is photolysed by UV radiation to produce one Cl atom and four oxygen atoms, either in their ground-state ($O(^3P)$) or in an excited state ($O(^1D)$). The breakdown chain proposed by Zhang et al. (2021) is as follows:

$$\begin{aligned} ClO_4^- + h\nu &\longrightarrow ClO_3^- + O \\ &\longrightarrow ClO_2^- + 2O \\ &\longrightarrow ClO^- + 3O \\ &\longrightarrow Cl^- + 4O \\ &\longrightarrow Cl + e + 4O. \end{aligned} \tag{5}$$

We modelled the total process, including the adsorption and subsequent hydration of anhydrous $Mg(ClO_4)_2$, as

$$(ClO_4)_2 + 6H_2O + h\nu \longrightarrow (ClO_4)\cdot 6H_2O + Cl + 4O, \tag{6}$$

where we assume in our model that all oxygen atoms released are in their ground-state, and do not include electron (e) chemistry. There are large uncertainties associated with the products of reaction (6). Zhang et al. (2021) did not provide constraints on the release rate of either Cl or O atoms, or measurements of gas-phase HCl within their chamber. The laboratory work described by Georgiou et al. (2017) also studied $Mg(ClO_4)_2$ under Mars conditions, but focused on radiolysis reactions. They found radiolysis was able to induce the production of OH, super-oxide radicals (O_2^-), and H_2O_2 on moistened perchlorate. For the sake of simplicity and due to a lack of quantitative laboratory measurements regarding Cl release from dust in Martian conditions, we limited our study to Cl and O atom releases from dust.

We describe reaction (6) as a heterogeneous rate coefficient that is derived for the first time in this paper using empirical studies from prior laboratory measurements. Adopting the form of Eq. (4), we used the thermal velocity of H_2O, v_{H2O}, and the unit surface area of dust, S, and selected a perchlorate mass percentage of 0.49% ($\alpha = 4.9{\times}10^{-3}$), consistent with the global

mean Cl^- surface abundance (Keller et al. 2006). We began by adopting the temperature independent uptake coefficient of H_2O onto Earth mineral dust measured in the laboratory study of Seisel et al. (2005): $\gamma = 6.20\times10^{-2}$. Because the hygroscopic growth of perchlorate displays a dependence on the environmental relative humidity (RH; Jia et al. 2018; Gu et al. 2017), we scaled the uptake coefficient by the atmospheric RH. Following Zhang et al. (2021), who reported the necessity of UV radiation to increase the oxidation rate of methane in their laboratory experiments, we scaled our model chlorine release rate by the photolysis rate of ClO (j_{ClO}, Table D.1). ClO was chosen because it is the final step in our model breakdown chain (Eq. (5)). The presence of ionising radiation has been reported by a laboratory study to accelerate the thermal decomposition of $Mg(ClO_4)_2$ (Devlin & Herley 1986). Due to the lack of global magnetic field and the thinner atmosphere, the Curiosity Rover receives a radiation dose rate of 233 ± 12 μGy day^{-1} (Matthiä et al. 2017), roughly 17 times more than that on Earth. The breakdown of perchlorate in dust grains could be accelerated further by the ionising radiation entering the atmosphere, which was not considered in the experiments of Zhang et al. (2021).

In summary, our uptake coefficient is defined as

$$\gamma_{h_{cl001}} = 6.20 \times 10^{-2} \times \mathrm{MIN}(\mathrm{RH}, 1.0) \times j_{ClO}. \quad (7)$$

2.3. Approach used to evaluate model HCl values

We compared the model HCl profiles resulting from the chlorine release mechanism described in Sect. 2.2 against 77 solar occultation retrievals of HCl from ACS/MIR in MY 34 (Korablev et al. 2021). For each model calculation, we initialised methane with a value of 20 pptv, consistent with the most recent upper limits reported by the ExoMars TGO (Knutsen et al. 2021; Montmessin et al. 2021), and all chlorine-containing gases with a value of 0 ppbv.

To evaluate our 1D model against TGO HCl measurements, we used atmospheric profiles of pressure, zonal and meridional winds, convective vertical wind variance (q2) for the vertical diffusion routines, and volume mixing ratio (VMR) profiles of CO_2, CO, O_2, and H_2 that have been interpolated from the Mars Climate Database v6.1 (Millour et al. 2015) Climatology datasets. Our interpolation routine takes into account altitude, planet latitude and longitude, solar longitude, and local time. We used optical opacity values from either the MCDv6.1 standard climatology (Montabone et al. 2015) or the MY34 climatology dataset (Montabone et al. 2020) for the calculation of photolysis frequencies in the chemistry.

To study each HCl retrieval from ACS/MIR, we used three model scenarios. The first uses the Standard Climatology datasets of the MCDv6.1 to drive the model, sampled at the latitude, longitude, and solar longitude of the relevant ACS/MIR HCl observations. The second uses the MY34 climatology dataset sampled at the latitude, longitude, and solar longitude of the ACS/MIR HCl retrieval.

The final scenario uses MY34 Climatology, but for each ACS/MIR HCl retrieval we took the nearest collocated dust and water ice mass loading (g cm^{-3}) and radii (μm) profiles from the thermal infrared (TIRVIM) and near-infrared (NIR) channels. We required the aerosol observations to be within ±5° latitude and ±10° solar longitude of the ACS/MIR HCl retrieval. In some instances, a simultaneous retrieval of H_2O was made by the ACS NIR channel (Fedorova et al. 2023). When no such retrieval was made, we used NOMAD H_2O profiles from MY 34 (Aoki et al. 2019) that match our collocation criteria. The reader is referred to Luginin et al. (2020) for a detailed description of the retrieval of aerosol optical properties and of the corresponding aerosol profiles for periods before, during the peak, and during the decay phases of the MY 34 global dust storm (L_S 170–255°). TIRVIM-NIR aerosol profiles measured during L_S = 255–338° are appear in this work for the first time, and are freely available from the Mendeley Data repository (Luginin 2022). The aerosols are radiatively inactive in our model, which we acknowledge will introduce an error in our photochemical calculations. In this scenario, we sampled the model at the latitude, longitude, and solar longitude of each ACS TIRVIM-NIR retrievals to provide the most appropriate model atmospheric temperature.

For dust mass mixing ratio (MMR) and radii profiles and H_2O VMR profiles in scenario three, our 1D model assumes that the profile shape below the lowest altitude of the ACS TIRVIM-NIR/NOMAD observations are the same as those in the MCDv6.1 dataset for the relevant latitude, solar longitude, and local time. We achieved this by scaling the climatology at lower altitudes by the ratio of observation:climatology where they begin to overlap in altitude. Above the TIRVIM-NIR upper altitude bound, the model assumes no dust or water ice is present. For all NOMAD H_2O profiles retrievals the upper altitude boundary exceeds the 1D model upper boundary of 70 km. For water ice profiles, we assumed the model has no ice below or above the altitude range of the TIRVIM-NIR measurements.

Our 1D model approximates diurnal variance in the aerosol and H_2O VMR interpolation schemes for scenario three. The column abundances of dust, ice, and H_2O across one Mars sol (48 timesteps) in the MCDv6.1 dataset are found, and normalised with respect to their value found at a 1D model local time closest to the ACS TIRVIM-NIR aerosol measurements. The aerosol and H_2O profiles at each altitude grid point are scaled by the resulting normalised values at each model timestep. This approach accounts for diurnal fluctuations in column abundances, but does not account for diurnal variances in profile shapes. Water ice profiles experience strong diurnal changes in profile shapes and abundance (Wu et al. 2022), which we acknowledge is a source of model error.

For each run, we initialised the model at the local time equal to the ACS/MIR HCl observations, and we spun up the model for 5 model sols. This is of similar magnitude to the lifetimes of HCl calculated in Fig. 1a, and allows the 1D model to produce output across a Martian sol that is self-repeating for the highly reactive HO_X (H, OH, and HO_2) and O_X (O and O_3) compounds. From this time onwards, HCl profile abundances change by <0.1% between successive iterations at local time 12:00. To evaluate our model, we used our model HCl profiles that correspond to the nearest time and location to the ACS/MIR retrievals on the sixth model sol.

3. Model evaluation using observed distributions of HCl

3.1. HCl vertical profiles

Figure 2 shows 1D model comparisons with three ACS/MIR observations within high northern latitudes (54.4–60.8° N), across L_S = 240.9–247.3°. We find that the 1D model is capable of reproducing both the vertical shape and abundances of some ACS/MIR HCl retrievals at high northern latitudes when it is driven by ACS TIRVIM-NIR aerosol and ACS NIR/NOMAD H_2O profiles (Figs. 2a,b). However, in some instances we find strong negative model HCl biases compared with ACS/MIR HCl retrievals despite the similarities in the profile shapes, namely the

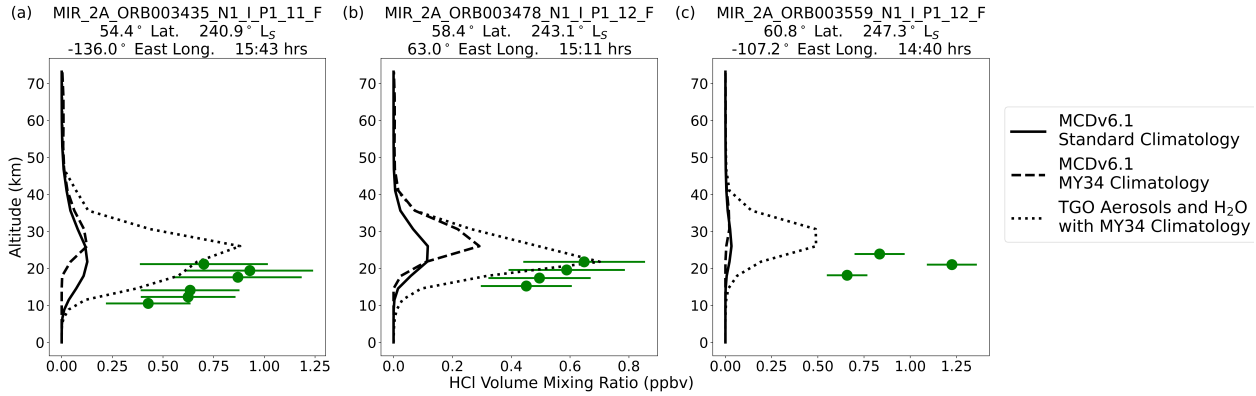

Fig. 2. Three exemplar ACS/MIR and 1D model HCl VMR values (ppbv) as a function of altitude in MY34 for high northern latitudes, defined here as ranging from 45°N to 75°N. Dotted red lines indicate model results when driven by aerosols and H_2O profiles from the 'Standard Climatological' MCDv6.1 dataset.

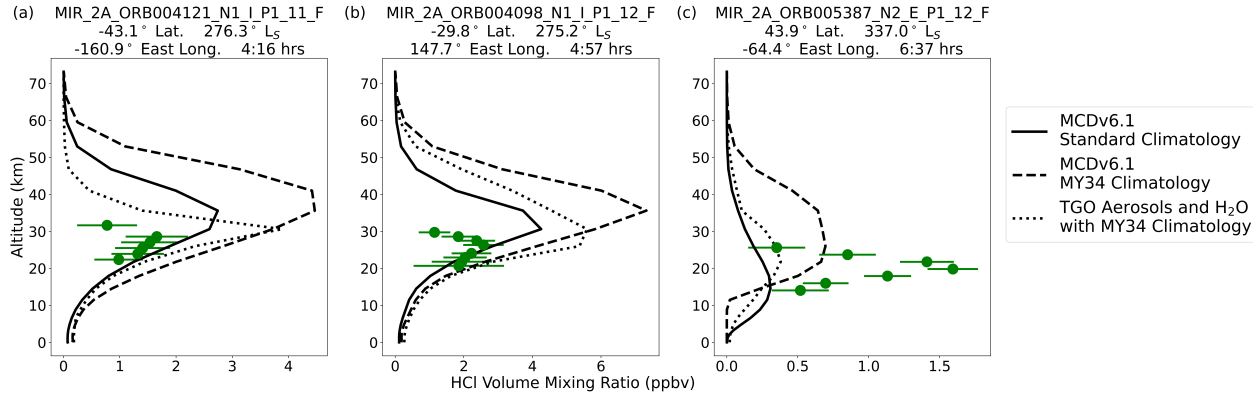

Fig. 3. Same as Fig. 2 but for latitudes within the tropics, defined here as ranging from 45°S to 45°N.

layered structure centred at 15–25 km altitudes shown in Fig. 2c. For some coincident profiles, the model HCl fails to exceed 100 pptv while ACS/MIR retrievals have a value of 1–2 ppbv. When driven by either the MCDv6.1 Standard or MY34 Climatology aerosols and H_2O, the layered structure is replicated in the northern latitudes but abundances typically suffer a 0.5–2 ppbv negative bias compared to the observations. One plausible explanation for the model discrepancies at these latitudes is the nature of the 1D model and its lack of horizontal transport. Korablev et al. (2021) and Aoki et al. (2021) both explain that meridional transport may be important for their observations in the high northern latitudes around perihelion. In this region at this time, the atmosphere is very dry and H_2O abundances are typically not high enough to enable our release mechanism to produce enough gas-phase chlorine. From Fig. 1a, HCl lifetimes reach 1–10 days within 5–35 km between 0 and 45° N between 180 and 330° L_S. This would enable HCl profiles in the north to be influenced by HCl blown in by winds flowing from the southern, wetter, and dustier regions. Kippenberger et al. (2019) also show HCl in Earth stratospheric conditions is capable of being trapped within growing water ice crystals. This process is not considered in our model – in reality, this could allow an additional source of HCl to be transported to the northern latitudes via the water ice on northward winds. When water ice sublimates, gas-phase HCl would then be reintroduced to the atmosphere.

Figure 3 shows three profile comparisons for latitudes within the Martian tropics (43.1° S–43.9° N). Observations of HCl from the ACS/MIR in this region are typically restricted to altitudes between 10 and 30 km. Driven with approximately colocated ACS TIRVIM-NIR aerosols and ACS NIR/NOMAD H_2O profiles, the 1D model often produces HCl in layers centred upon 10–30 km with abundances that are consistent with the ACS/MIR observations.

Figures 3a–c show that the model is able to reproduce the profile shapes of ACS/MIR HCl when driven with all three climatological scenarios. In all figures, the model produces HCl above TGO detection levels (0.1 ppbv) at altitudes greater than 30 km. This is not corroborated by the ACS/MIR observations. In Figs. 3a and b, the HCl maxima appears 5–10 km higher than the maxima of the ACS/MIR observation with both standard and MY34 MCDv6.1 climatology runs. When driven with colocated H_2O and aerosol profiles retrieved by NOMAD/ACS NIR and ACS TIRVIM, the model layer altitudes are in agreement with the ACS/MIR. The southern latitude layers (Figs. 3a and b) tend to form at higher altitudes than in the north (Fig. 3c), a phenomena replicated by the 1D model. Despite small positive model biases (1–4 ppbv) existing in the southern latitudes, and negative model biases (0.5–1 ppbv) in the north, the model reproduces the distribution of observed HCl within the tropics in MY 34.

Figure 4 shows three profile comparisons from high southern latitudes (73.6°–48.0° S). In Fig. 4a (48° S) the ACS/MIR HCl profiles still include a layered formation, but with a less pronounced cutoff at lower altitudes – the abundances tend to be slightly more homogeneous towards the surface. This behaviour is reproduced by the 1D model driven by the proposed chlorine release mechanism across all three climatology scenarios. The model qualitatively reproduces the HCl vertical distribution

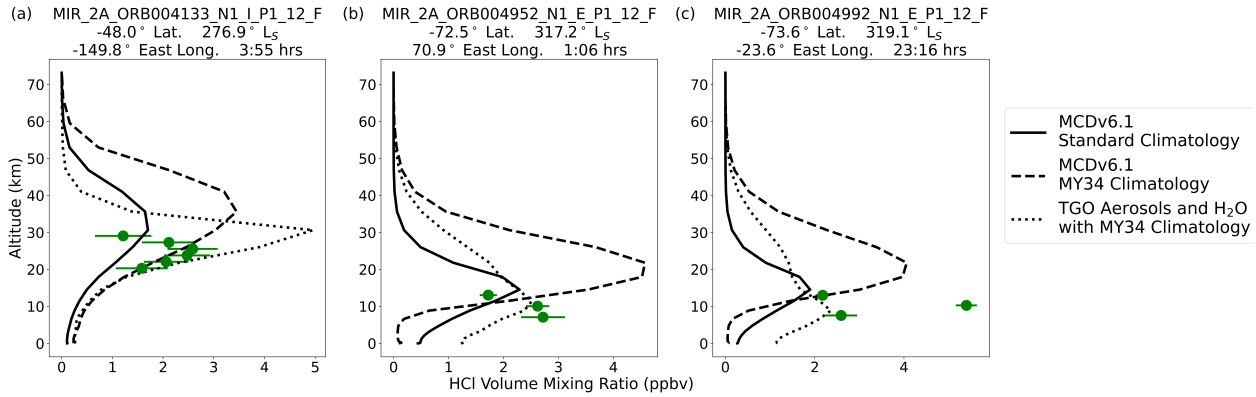

Fig. 4. Same as Fig. 2 but for high southern latitudes, defined here as ranging from 75°S to 45°S.

but with a model bias of approximately 2 ppbv when we used colocated ACS TIRVIM aerosol and NOMAD/ACS NIR H_2O profiles. In Figs. 4b and c (72.5° and 73.6° S), HCl tends to be confined below altitudes of 30 km due to the widespread presence of water ice clouds above 20 km, with HCl VMRs that range between 2 and 6 ppbv. The lack of dust above 20 km also contributes to the suppression of HCl to altitudes below 20 km as observed by ExoMars TGO instrumentation. Using the climatological MCDv6.1 aerosols and H_2O profiles, the 1D model reproduces the high southern latitude HCl shape and abundances.

Generally, we find that our proposed chlorine release mechanism, as described above reproduces the abundances, vertical and horizontal distributions of ACS/MIR HCl observations in MY34. When driven with standard climatological or MY34 datasets from the MCDv6.1, we find that the model has a negative biases at high northern latitudes (Fig. 2) and the model produces HCl above the altitude range observed by the TGO (Figs. 3 and 4). When we use colocated aerosol profiles from the ACS TIRVIM and H_2O profiles from NOMAD/ACS NIR, we find that the model generally does a better job at describing the magnitude and distribution of ACS/MIR HCl observations at all latitudes.

3.2. Similarity between HCl and H_2O profile shapes

The shapes (normalised vertical distributions) of the retrieved HCl profiles are correlated to the profile shapes of colocated H_2O (Korablev et al. 2021; Olsen et al. 2021; Aoki et al. 2021). The true H_2O and HCl VMR abundances are different by 3–4 orders of magnitude, which motivated Aoki et al. (2021) to apply a scaling method to their H_2O profiles, an approach we adopted here.

The scaling factor for each H_2O profile is the ratio of the partial column densities of HCl and H_2O through altitudes below 25 km where HCl is observed. For these calculations, the total atmospheric number densities are found using pressure and temperature profiles from the climatological MCDv6.1 datasets. Each point on the H_2O profile is then multiplied by the resulting scaling factor.

Figure 5 presents the resulting scaled H_2O VMRs and colocated HCl VMRs retrieved by the NOMAD instrument across MY34–35, following Aoki et al. (2021), and those from the 1D model when driven by the three climatology scenarios, detailed in Sect. 2.3, used to produce the 77 ACS/MIR observation comparisons from Sect. 3.1. The values plotted for the 1D model are extracted within the altitude range of 7.5–35.5 km,

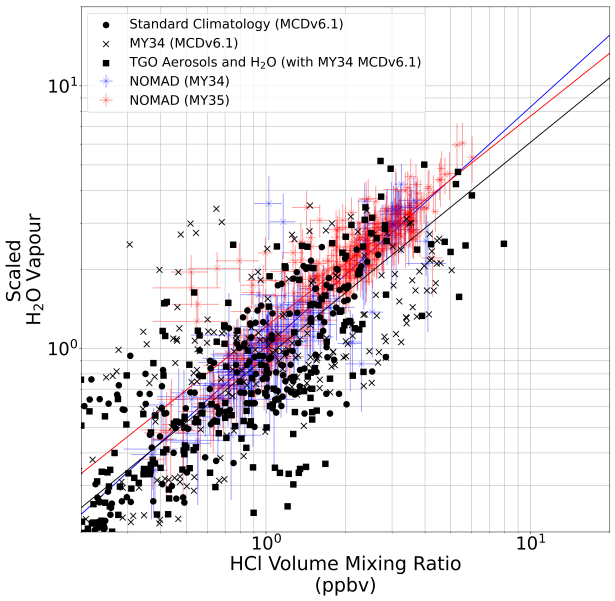

Fig. 5. Comparisons of the normalised HCl and H_2O VMR abundances observed by the NOMAD spectrometer in MY34–35 (Aoki et al. 2021) and the 77 1D photochemistry model runs with the standard climatological and MY34 datasets of the MCDv6.1, and MY34 with approximately colocated ACS TIRVIM aerosols and NOMAD/ACS NIR H_2O profiles. Gradients (m) and correlation coefficients (R) for the lines of best fit are as follows. For all model runs, m = 0.82 and R = 0.854. For NOMAD MY34, m = 0.91 and R = 0.92. For NOMAD MY35, m = 0.80 and R = 0.90. This analysis follows Aoki et al. (2021).

corresponding to the mean altitude range observed by Aoki et al. (2021) ± the standard deviation for the lower and upper bounds, respectively. We excluded model HCl VMRs below the detection limit of 100 pptv.

In Fig. 5, we show the 1D model HCl VMRs and the scaled H_2O VMRs, retrieved by ACS NIR/NOMAD used to drive the model, reproduce the fit originally described by Aoki et al. (2021). Driving the model with all three climatology scenarios maintains a good agreement with data collected by the NOMAD instrument.

Cl atom release is dependent on the number density of H_2O in the atmosphere in our model calculations through the heterogeneous rate coefficient (Eq. (4)). When ejected in the gas phase, Cl atoms require additional reactions with either HO_2 or H_2 to produce gas phase HCl. Because HO_2 is dependent on the UV photolysis of H_2O to produce HO_X compounds in

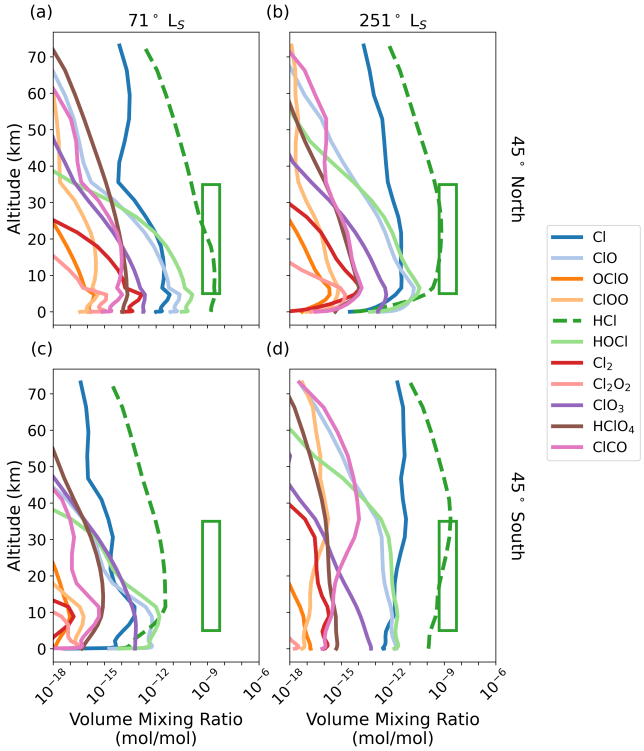

Fig. 6. Volume mixing ratios of all chlorine species from the 1D model at aphelion (71° L_S) and perihelion (251° L_S), at 45° N (a and b) and 45° S (c and d). The green box displays the range of HCl VMRs observed by Korablev et al. (2021) and Olsen et al. (2021) from 5–35 km.

the atmosphere, H_2O controls the chemical production of the two reactants that enable HCl production (Cl and HO_2, cl_9 in Table D.3). The destruction of HCl is determined mainly by heterogeneous uptake on water ice (Figs. 1b and c). The abundances of H_2O and water ice display an anti-correlation due to condensation and sublimation (Poncin et al. 2022). As a consequence, the loss rate of HCl will be negatively correlated with H_2O abundances. Together, this results in HCl being strongly dependent on H_2O in our model, and explains the strong coincidences in HCl and H_2O abundances displayed in Fig. 5.

3.3. Seasonal cycle of chlorine chemistry

Figure 6 shows the 1D model VMR profiles of all chlorine species, with maximum VMRs greater than 10^{-18} mol mol^{-1}, when driven by standard climatological aerosols, temperature profiles, and H_2O from the MCDv6.1. The profiles correspond to aphelion and perihelion solar longitudes and to latitudes 45° N and 45° S. All of the 1D model runs use the same spin-up period of 5 sols before extracting the profiles at a local time of 18:00, corresponding to the time of a typical solar occultation profile retrieval.

For the northern hemisphere at aphelion (Fig. 6a) our proposed chlorine release mechanism produces abundances of HCl between 0.1 and 2.6 ppbv between 5.0 and 20 km. This lies within the observational window of ACS/MIR indicated by the green rectangle. Detections of HCl between L_S 0 and 180° are infrequent. However, a study has reported a retrieval of a HCl profile with a layered structure of 1–2 ppbv centred between 5 and 10 km at 46° N, L_S 115° in MY35 (Olsen et al. 2021), which is consistent with our 1D model calculations.

For the northern hemisphere at perihelion (Fig. 6b), the 1D model produces a maximum of 600 pptv HCl between 10 and 30 km. This low level of photochemical production is also shown in Fig. 2c. The model does reproduce the layered HCl structure that declines rapidly below 20 km. Below 5 km, the 1D model suggests that ClO becomes the dominant chlorinated tracer, although at values of less than 100 pptv it is below the limit of detection for TGO instruments.

For the southern hemisphere at aphelion (Fig. 6c), the HCl abundances are orders of magnitude lower than elsewhere. Maximum HCl VMRs do not exceed 10 pptv within the range of altitude measurements. Below 10 km, ClO is the dominant chlorinated tracer with values <10 pptv. Values of HOCl, atomic Cl, and ClO_3 are produced at similar amounts to HCl. For the southern hemisphere at perihelion, the sublimating polar ice caps enable HCl in the southern hemisphere (Fig. 6d) to increase to 1–10 ppbv, where they form a layered structure. The reduction in HCl at lower latitudes is less pronounced than in the northern hemisphere at perihelion (Fig. 6b). This supports the HCl observations reported for MY34 and MY35 made by Korablev et al. (2021) and Olsen et al. (2021). However, abundances are higher than 100 pptv up to altitudes of 40–45 km. The ACS/MIR did not report observations of HCl above 25 km in the deep southern latitudes (Korablev et al. 2021; Olsen et al. 2021).

3.4. Coincidences of holes in ice clouds with HCl profiles

A recent study has presented evidence of an anti-correlation between HCl and water ice abundances using profiles retrieved from the ACS instrument (Luginin et al. 2024). ACS TIRVIM found that when water ice clouds form in two layers, separated by an absence of ice (an 'ice hole'), HCl concentrations become elevated. Figure 7 shows our 1D model HCl values, corresponding to ACS/MIR retrievals (Sect. 3.1) for which there is an ice hole structure present, driven by ACS TIRVIM-NIR aerosols and ACS NIR/NOMAD H_2O profiles to recreate the ACS/MIR observations from Sect. 3.1. The HCl and water ice profiles are normalised, and the altitude corresponding to the centre of each ice hole is found. The normalised profiles are then plotted, with the Y-axis corresponding to the distance from the ice hole centre. We find that strong uptake on water ice causes HCl to reach maximum values within the ice holes observed by ACS TIRVIM, a phenomena that corroborates the findings of Luginin et al. (2024). Without the presence of strong heterogeneous uptake on water ice, the HCl lines displayed in Fig. 7 would be significantly flatter.

3.5. Qualitative summary of the model HCl cycle

During the first half of the northern spring (L_S 0–45°), the atmosphere is quite dry across the planet. Dust is ubiquitous, but at low abundances and confined to altitudes below 20 km. The lack of H_2O to efficiently trigger Cl release from dust results in a low photochemical production of HCl. HCl that is produced is quickly scavenged by adsorption onto the dust grains. Any HCl that survives and diffuses upwards is removed via water ice crystals above 20 km. As a result, no HCl is found by TGO instrumentation across the planet throughout L_S 0–45°.

HCl remains below detection limits (100 pptv) until the start of the northern summer (L_S 90°). At this time, the northern polar cap begins to sublimate and release H_2O at high concentration. In high northern latitudes, H_2O abundances rapidly hydrate the low dust abundances found below 10 km, and extended exposure to UV radiation enables strong Cl releases to occur in our

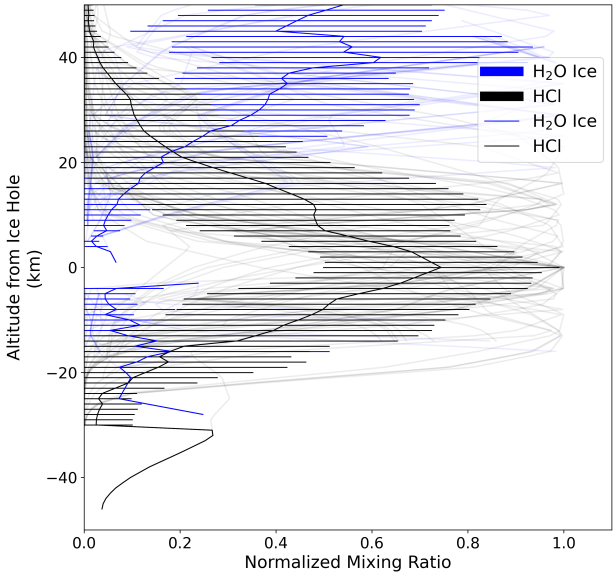

Fig. 7. Normalised HCl profiles produced by our 1D photochemical model, driven by approximately colocated water ice profiles measured by ACS TIRVIM (presented in blue) and NOMAD/ACS NIR measured H_2O profiles. Semi-transparent lines are individual profiles, and the opaque lines represent the mean and standard deviation of the plotted profiles. The profiles are centred on the altitude corresponding to the centre of the ice holes; the maximum HCl abundances calculated by the model closely coincide with the locations of the ice holes.

model. The strong Cl release produces HCl from the photochemical products of photolysed H_2O. Temperatures below 20 km prevent water ice clouds forming below 20 km, a gap that enables HCl to develop to 1–10 ppbv below 20 km in the northern latitudes between L_S 90 and 180°. At the equator and in the southern hemisphere, temperatures are lower and H_2O condenses to water ice above 5 km. This causes HCl to remain below 100 pptv below 30° N in the northern summer.

As Mars enters northern autumn (L_S 180–270°), the high northern latitudes begin to cool and H_2O condenses and falls to <100 ppmv below 20 km. Water ice abundances reach magnitudes of 10^0–10^1 ppmv below 20 km, providing a strong sink for HCl – the lower H_2O also enables less Cl to be released, and HCl does not form above TGO detection limits. However, TGO does report HCl here at 0.1–3 ppbv. In the high northern latitudes, the temperatures between 20 and 50 km rise due to meridional winds from the south, which causes water ice to sublimate. The lack of ice in this window would enable HCl produced in lower latitudes to be transported northwards and be measured by TGO instruments. We hypothesise that HCl observed by the TGO instruments during the northern autumn in the northern pole is a result of production in the dustier and wetter equatorial regions, and transported meridionally to the north.

Northern autumn also marks the start of the dust season, where dust mixing ratios in the tropics reach 10^1 ppmv magnitudes as high as 50 km in the tropics and high southern latitudes. Water ice in the southern polar cap also begins to sublimate in the higher atmospheric temperatures. In the equatorial regions, H_2O develops a layered structure with maxima of 100–200 ppmv centred on 20–40 km. This H_2O hydrates the airborne dust, and enables Cl atoms to be ejected from the dust and HCl to form from atmospheric photochemistry. Water ice forms above 40 km, and also below 15 km in the northern hemisphere. This forces HCl to form a layer centred on 30–40 km. In the southern hemisphere, the layer forms due to the profile shape of H_2O, and the lack of ice below 15 km makes the cutoff at 20 km less sharp than in the north.

As the dust season ends (L_S 315°), the atmosphere becomes drier as temperatures begin to fall. Less hydration of perchlorate occurs, causing Cl release rates to fall, and HCl is scavenged by heterogeneous uptake by the dust that remains. By the end of the Mars year (L_S 350–360°), HCl falls to below TGO detection limits across the globe, and the cycle starts anew.

3.6. Impacts on methane's photochemical lifetime and ozone

A potentially important consequence of chlorine chemistry on Mars, as evidenced by the presence of HCl, is its ability to react with methane and consequently shorten the atmospheric lifetime of methane. At temperatures of 200 K, the reaction of methane with Cl atoms (1.3×10^{-14} cm^3 mol^{-1} s^{-1}, Burkholder et al. 2019) is about forty times faster than with OH (3.3×10^{-16} cm^3 mol^{-1} s^{-1}, Burkholder et al. 2019). Chlorine chemistry is also highly influential on Earth's atmospheric O_3, a species regularly observed on Mars by satellites and used to constrain Martian HO_X chemistry. To study the impact of our chlorine release mechanism on atmospheric methane and O_3, we drove the 1D model with climatological tracers and atmospheric parameters from the MCDv6.1. We performed 1D model runs for latitudes 60° S to 60° N in intervals of 30°, using the same solar longitude grid as shown in Fig. 1a. For all 1D model runs, we assumed a fixed homogeneous methane profile of 20 pptv. We used a spin-up period of 5 sols to match the magnitude of the HCl lifetime in the model.

Figure 8a shows the ratios of the column integrated photochemical lifetime of methane in 1D model runs without chlorine chemistry (control run), and those calculated with our chlorine release mechanism active. Figure 8b shows the ratio of the atmospheric column of O_3 between the chlorine-active run and the control run. Figures 8c and d present vertical profiles of CH_4's atmospheric lifetime and the O_3 VMR at local times of 12:00 h and 18:00 h (approximate time for solar occultation measurements to be made), respectively. Profiles at latitudes of 45° N, 0° N, and 45° S are shown at perihelion (251°).

We find that including our chlorine release mechanism results in the column integrated lifetimes of methane decreasing from >100 yr to between 1 and 10 yr between 30° S and 30° N below 20 km throughout L_S 60–180°. This corresponds to increases in the loss rate of atmospheric methane that are one to two orders of magnitude higher than through conventional gas-phase photochemistry. During the dusty season (L_S 180–360°), the methane lifetimes remain below 10 yr below the dust top at 20 km. The 1D model column and profile abundances of our organic oxidation products (Table C.1) remain below 1 pptv. Formic acid (HCOOH) columns reach 2.00×10^{-14} mol mol^{-1}, formaldehyde (HCHO) columns reach 2.40×10^{-15} mol mol^{-1}, and methanol columns peak at 6.94×10^{-16} mol mol^{-1}. Halogenated organics, including methyl chloride (CH_3Cl) and methyl hypochlorite (CH_3OCl) remain at values (2.31×10^{-18} and 1.62×10^{-18} mol mol^{-1}, respectively) that are far below the ACS revised upper limit of 1 ppbv (Trokhimovskiy et al. 2022). The production of Cl atoms from dust, water, and UV photon interactions could therefore also be a major chemical sink for organic species on Mars. Whether methane is present in the Mars atmosphere remains a subject of debate, but we show how chlorine chemistry would help explain why methane is not detected in the upper atmosphere by orbiting satellites and how methane at the surface, as observed by Curiosity's SAM instrument (Webster et al. 2013, 2018), could sustain a seasonal cycle.

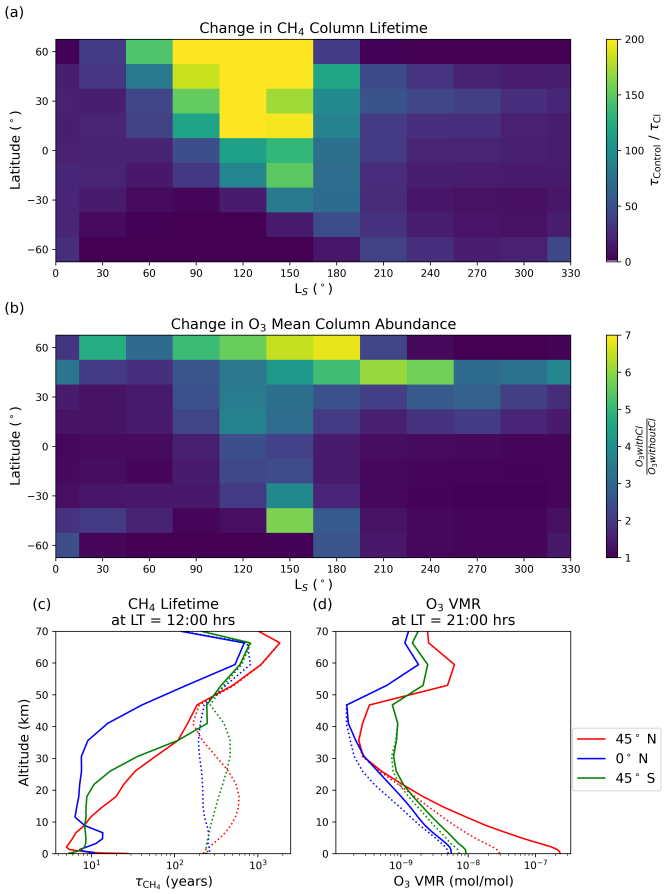

Fig. 8. Impacts of the chlorine release mechanism proposed in this work on the atmospheric lifetime of CH_4 and the abundances of O_3 across latitudes 60° S – 60° N and L_S 0–360°. The 1D model is driven by MY34 climatological datasets from the MCDv6.1, positioned at longitude 0° E. (a) Ratio of the column lifetime of CH_4 without chlorine chemistry ($\tau_{Control}$) and the column lifetime with chlorine chemistry (τ_{Cl}). (b) Ratio of the O_3 column abundances with chlorine chemistry and without chlorine chemistry at LT = 12:00 h. (c) CH_4 lifetime profiles with (solid) and without (dashed) chlorine chemistry at L_S 251°. (d) O_3 VMR profiles with (solid) and without (dashed) chlorine chemistry at L_S 251°.

The impacts of chlorine chemistry on the model O_3 profiles is limited to altitudes below 20 km. In high northern latitudes during perihelion and the sublimation of the northern ice cap, the 1D model with chlorine release active produces O_3 column densities that are 4–6 times higher than the control runs. This is due to our reaction scheme that introduces four $O(^3P)$ atoms alongside each released Cl atom (Eq. (6)). The impact on the column abundances decreases in the dust season (L_S 180–330°), with equatorial O_3 column abundances increasing by factors of 1–2. NOMAD has observed O_3 profiles to altitudes of 5–10 km (Patel et al. 2021). It was found that chemical models throughout the northern hemisphere in the non-dusty season (L_S 0–180°) produce negative biases in their O_3 profiles of factors of 2–10 below 30 km compared to the NOMAD retrievals. The additional O atoms introduced by our chlorine release scheme could be capable of improving our chemical modelling abilities of the Martian O_3 cycle.

4. Discussion

Here, we describe some of the shortcomings of our study, including caveats associated with our modelling of heterogeneous chemistry, over-production of HCl during the northern hemisphere summer relative to TGO measurements, and finally an evaluation of our results against previous studies.

4.1. Limitations of modelling heterogeneous chemistry

Our model chemistry does not consider solid-state products within or on the surface of aerosols. The long-term impacts of soil chemistry on chlorine must be investigated, and we recommend that the chemistry of Martian soil analogies be studied via laboratory experiments, for example Mars Global Simulant 1 (Cannon et al. 2019) spiked with appropriate levels of perchlorates, salts, and super oxides. This will help constrain possible reaction rates, and address whether chlorine in the soil can be maintained at levels observed by in situ instruments such as the Phoenix and Viking landers (Hecht et al. 2009; Clark et al. 1982) and the Curiosity Rover (Thomas et al. 2019) while releasing chlorine as described in our study.

We can estimate the lifetime of perchlorate within the dust in our model by considering the total column values of the release rate of Cl atoms and the mass of Cl within the dust grains. For the 77 1D model runs performed with ACS TIRVIM aerosols and ACS NIR/NOMAD H_2O profiles, the column release rate of Cl ranges between 2.45×10^6 and 9.26×10^{11} Mol cm^{-2} s^{-1}, with mean rate of 1.1×10^{11} mol cm^{-2} s^{-1}. Dust-trapped Cl atom column densities are calculated by finding the column mass of dust in g cm^{-2} and multiplying by the global mean Cl^- concentration of 0.49×10^{-3} (Keller et al. 2006). These values range from 5.14×10^{14} to 5.80×10^{16} mol cm^{-2} with a mean value of 1.17×10^{16} mol cm^{-2}. Division of the Cl^- column concentrations with the column release rates produces dust-bound perchlorate lifetime estimates that range between 10^2 and 10^4 days. The stability of perchlorate within the Martian soil across geological timescales becomes questionable in this scheme. Future investigations using models should include full 3D transport, and should track the chlorine-content of the soil as a separate tracer species.

Similarly, our description of heterogeneous uptake of HCl onto water ice does not consider the chemical products on the ice surface. This will inevitably result in a mass imbalance when applied to a global 3D general circulation mode, and should be considered in future work. We accounted for saturation of uptake sites by using the non-dissociative Langmuir model (Eq. (2)). We accounted for the photolysis of HCl adsorbed on the ice surface by reintroducing Cl and H atoms into the atmosphere at the rate at which the HCl is taken up by the ice surface during daytime conditions. We acknowledge this approach will overestimate the rate at which HCl photolyses on the ice surface. When adsorbed onto growing ice crystals, HCl is capable of being buried in the ice (Kippenberger et al. 2019). The sublimation of ice may also contribute additional HCl to the northern and southern polar latitudes during the dust-storm, which our studies currently underestimate (Figs. 2 and 4).

4.2. Over-production of HCl in the northern hemisphere summer

The equation we used to describe the rate of chlorine release (Eq. (7)) does not account for saturation of the aerosol. As water is adsorbed, competition for free uptake sites can be expected to hinder the rate of uptake. This will result in overestimating the release rate of Cl atoms. This error is most noticeable in model runs at latitudes higher than 45° N during northern hemisphere summer months (L_S 90–180°), where HCl can be produced at

1–10 ppbv abundances below 20 km. The sublimation of surface water ice in the northern pole introduces more H_2O to the atmosphere during this period than the southern pole does during its summer period (L_S 270–360°). Accounting for dust saturation is necessary to improve upon the accuracy of this modelling approach.

4.3. Comparison with previous studies

Impacts of chlorine chemistry on Martian atmospheric methane as reported in this study differs from previous modelling efforts. Krasnopolsky (2022) uses another 1D model to calculate a decrease of 10^0–10^1 in the lifetime of atmospheric methane. In their model, chlorine is produced by gas-phase O and H reactions with airborne dust minerals, which release ClO and HCl, respectively. The resulting Cl atom abundances in their model are then produced via photolysis of halogenated gas-phase species. In our model, we directly release Cl atoms from the dust grains. We also find that when we drive our model with TGO aerosol and H_2O profiles, Cl atom number densities can reach concentrations of 10^4–10^5 mol cm^{-3} below 20 km, which are 1–2 orders of magnitudes higher than those reported by Krasnopolsky (2022). Above 20 km, Cl atom densities in our model fall to 10^2–10^4 mol cm^{-3}, whereas Krasnopolsky (2022) see Cl rise to between 10^5 and 10^6 at 60 km (Fig. 6).

Grenfell et al. (2022) also find a small impact of chlorine chemistry on atmospheric methane, resulting in a photochemical lifetime decrease of a factor of 6.0 with respect to conventional organic photochemistry. Their steady-state model was established with a surface HCl flux of 2.4×10^4 mol cm^{-2} s^{-1} to produce a surface HCl VMR of 2 ppbv. Their source of Cl atoms is the photolysis of halogenated gas, similar to Krasnopolsky (2022). Their model did not include heterogeneous uptake of HCl and only considered conventional gas-phase chemistry. This approach results in surface Cl atom VMRs of 10^{-14} mol mol^{-1}, which rise to 10^{-10} mol mol^{-1} at 40 km. Figures 6b and d show that our 1D model calculates Cl atom VMRs can reach 10^{-13}–10^{-11} during the perihelion season in the northern and southern hemispheres.

5. Conclusions

Motivated by recent studies that have reported observations of HCl in the Martian atmosphere (Korablev et al. 2021; Olsen et al. 2021; Aoki et al. 2021), we propose a heterogeneous chemistry network to describe the corresponding production and loss of atmospheric HCl. Our approach was inspired by a laboratory study that reported hydrated magnesium perchlorate under UV radiation that enhanced the oxidation rate of methane in an experimental chamber (Zhang et al. 2021).

Our key results include:

- The release of Cl atoms from the UV photolysis of hydrated perchlorate (motivated by the laboratory findings of Zhang et al. 2021) in airborne Martian dust, coupled with a strong heterogeneous uptake onto water ice particles and $CaCO_3$ within dust grains, is capable of reproducing the profile shapes and abundances of gas-phase HCl observed during the MY34 dust storm by the ACS/MIR (Korablev et al. 2021; Olsen et al. 2021);
- This release of Cl atoms is also able to reproduce the strong observed similarity between the vertical profile shapes of H_2O and HCl (Korablev et al. 2021; Olsen et al. 2021; Aoki et al. 2021). This is demonstrated in Fig. 5, which shows that 1D model HCl values, driven by ACS TIRVIM aerosols and ACS NIR/NOMAD H_2O, follow the broad vertical distribution of observed H_2O profiles;
- Our model, when driven with ACS TIRVIM aerosol profiles, was able to reproduce the observed sharp vertical gradients in HCl associated with water ice layers (Luginin et al. 2024). When there were rapid vertical reductions in the water ice content – so-called ice holes (Fig. 7) – we found commensurately rapid increases in HCl. This is consistent with our assumed efficient uptake of HCl on water ice and with the observed relationship between ACS retrievals of HCl and water ice (Luginin et al. 2024);
- Our proposed mechanism that describes the uptake of HCl on ice – which includes an empirically derived temperature-dependent uptake coefficient (Hynes et al. 2001) that is scaled to account for reversible uptake reactions and uptake site saturation – results in HCl column lifetimes that span 1–24 h. This is significantly faster than the lifetime of around 100 sols as predicted when using only gas-phase chemistry, and more in line with the upper limit of 75 sols that is needed to explain the rapid disappearance of HCl after strong dust events, as observed by TGO instrumentation;
- Finally, the Cl atoms being released from dust via our proposed mechanism, which produce 1–10 ppbv of HCl in climatological atmospheric conditions, also affects the wider atmospheric network. In particular, the elevated atmospheric Cl reduces the lifetime of atmospheric methane by 1–2 orders of magnitude relative to photochemical calculations that do not consider Cl. If methane is indeed on Mars, as reported by the Curiosity Rover, its gas-phase destruction via Cl released from dust grains could help corroborate these detections and explain the non-detections reported by orbiters such as the TGO.

We acknowledge that we have made and described a number of assumptions and caveats in our approach to describing atmospheric HCl on Mars. As such, we recommend further laboratory studies of the UV-activated release of chlorine from hydrated perchlorate for the range of atmospheric pressures, temperatures, and humidities experienced on Mars. This will allow us to refine the release rate of chlorine and the subsequent atmospheric chemistry. Including our model chemistry in a 3D general circulation model and tracking the chlorine budget of the soil will enable the longevity of the proposed chemistry mechanism to be better assessed. Improving the modelling of the heterogeneous loss of HCl onto water ice and tracking the HCl buried in ice crystals and subsequently released upon sublimation (in an approach similar to that employed by Brown et al. 2022 for OH onto ice) will provide improved modelling results for the dry environments of the polar latitudes during their respective winters.

Acknowledgements. This research was funded in part by the UK Space Agency (UKSA) [ST/1/R001324/1], administered by the Science and Technology Facilities Council, as part of the Aurora science programme. For the purpose of open access, the author (B. Taysum) has applied a creative commons attribution (CC BY) licence to any author accepted manuscript version arising. P.I. Palmer acknowledges funding from the UKSA (ST/Y003284/1). K.S. Olsen acknowledges funding from the UKSA (ST/T002069/1 and ST/Y000196/1). The ACS instrument was designed, developed, and operated by A. Trokhimovskiy, A. Shakun, A. Grigoriev, F. Montmessin, and O. Korablev. ACS TIRVIM-NIR data were calibrated by N. Ignatiev. Vertical profiles of dust and water ice properties from ACS TIRVIM-NIR and ACS NIR data were retrieved by M. Luginin. Vertical profiles of HCl from ACS/MIR were retrieved by K.S.O and were originally published in Korablev et al. (2021), the data of which are found in Olsen (2021). Vertical profiles of water vapour were retrieved and originally published in Fedorova et al. (2023), stored at Fedorova (2022). Retrievals of HCl by the TGO NOMAD spectrometer used in Fig. 5 were published in Aoki et al. (2021).

References

Abbatt, J., Beyer, K., Fucaloro, A., et al. 1992, J. Geophys. Res.: Atmos., 97, 15819
Altheide, T., Chevrier, V., Nicholson, C., & Denson, J. 2009, Earth Planet. Sci. Lett., 282, 69
Aoki, S., Richter, M., DeWitt, C., et al. 2018, A&A, 610, A78
Aoki, S., Vandaele, A. C., Daerden, F., et al. 2019, J. Geophys. Res.: Planets, 124, 3482
Aoki, S., Daerden, F., Viscardy, S., et al. 2021, Geophys. Res. Lett., 48, e2021GL092506
Atkinson, R., Baulch, D., Cox, R., et al. 2001, IUPAC Subcommittee on gas kinetic data evaluation for atmospheric chemistry, 20
Atkinson, R., Baulch, D., Cox, R., et al. 2007, Atmos. Chem. Phys., 7, 981
Banerdt, W. B., Smrekar, S. E., Banfield, D., et al. 2020, Nat. Geosci., 13, 183
Berho, F., Rayez, M.-T., & Lesclaux, R. 1999, J. Phys. Chem. A, 103, 5501
Berland, B., Tolbert, M., & George, S. 1997, J. Phys. Chem. A, 101, 9954
Boynton, W., Ming, D., Kounaves, S., et al. 2009, Science, 325, 61
Braude, A. S., Montmessin, F., Olsen, K. S., et al. 2022, A&A, 658, A86
Brown, M. A. J., Patel, M. R., Lewis, S. R., et al. 2022, J. Geophys. Res.: Planets, 127, e2022JE007346
Burkholder, J. B., Sander, S. P., Abbatt, J., et al. 2019, JPL Publication 19-5 (Pasadena: Jet Propulsion Laboratory)
Cannon, K. M., Britt, D. T., Smith, T. M., Fritsche, R. F., & Batcheldor, D. 2019, Icarus, 317, 470
Catling, D. C., Claire, M. W., Zahnle, K. J., et al. 2010, J. Geophys. Res.: Planets, 115, E00E11
Chevrier, V. F., & Rivera-Valentin, E. G. 2012, Geophys. Res. Lett., 39, L21202
Chevrier, V. F., Rivera-Valentín, E. G., Soto, A., & Altheide, T. S. 2020, Planet. Sci. J., 1, 64
Clark, B. C., Baird, A. K., Weldon, R. J., et al. 1982, J. Geophys. Res.: Solid Earth, 87, 10059
Daerden, F., Crowley, J. N., Neary, L., et al. 2023, J. Geophys. Res. (Planets), 128, e2023JE008014
Devlin, D. J., & Herley, P. J. 1986, Thermochim. Acta, 104, 159
Diez, B., Feldman, W. C., Mangold, N., et al. 2009, Icarus, 200, 19
Economou, T. 2001, Radiat. Phys. Chem., 61, 191
Edwards, C. S., & Piqueux, S. 2016, Geophys. Res. Lett., 43, 8912
Encrenaz, T., Bézard, B., Greathouse, T. K., et al. 2006, in Ground-based high-resolution IR spectroscopy of Mars: H2O and H2O2 mapping, search for CH4, and determination of CO2 isotopic ratios, Second workshop on Mars atmosphere modelling and observations, 511
Eskola, A. J., Timonen, R. S., Marshall, P., Chesnokov, E. N., & Krasnoperov, L. N. 2008, J. Phys. Chem. A, 112, 7391
Farley, K., Martin, P., Archer Jr, P., et al. 2016, Earth Planet. Sci. Lett., 438, 14
Fedorova, A. 2022, Water vapor saturation state on Mars from ACS-NIR/TGO occultations from MY34 to MY36, Mendeley Data, V1
Fedorova, A., Montmessin, F., Trokhimovskiy, A., et al. 2023, J. Geophys. Res.: Planets, 128, e2022JE007348
Fisher, D., Hecht, M., Kounaves, S., & Catling, D. 2008, in AGU Fall Meeting Abstracts, 2008, U11B-0019
Forget, F., Hourdin, F., Fournier, R., et al. 1999, J. Geophys. Res.: Planets, 104, 24155
Formisano, V., Atreya, S., Encrenaz, T., Ignatiev, N., & Giuranna, M. 2004, Science, 306, 1758
Gellert, R., Rieder, R., Anderson, R. C., et al. 2004, Science, 305, 829
Geminale, A., Formisano, V., & Giuranna, M. 2008, Planet. Space Sci., 56, 1194
Geminale, A., Formisano, V., & Sindoni, G. 2011, Planet. Space Sci., 59, 137
Georgiou, C. D., Zisimopoulos, D., Kalaitzopoulou, E., & Quinn, R. C. 2017, Astrobiology, 17, 319
Glotch, T. D., Bandfield, J. L., Wolff, M. J., Arnold, J. A., & Che, C. 2016, J. Geophys. Res. (Planets), 121, 454
Gough, R., Chevrier, V., Baustian, K., Wise, M., & Tolbert, M. 2011, Earth Planet. Sci. Lett., 312, 371
Gough, R., Chevrier, V., & Tolbert, M. 2014, Earth Planet. Sci. Lett., 393, 73
Grenfell, J. L., Wunderlich, F., Sinnhuber, M., et al. 2022, Icarus, 382, 114940
Gu, W., Li, Y., Tang, M., et al. 2017, RSC Adv., 7, 46866
Hanson, D. R., & Ravishankara, A. 1992, J. Phys. Chem., 96, 2682
Hartogh, P., Jarchow, C., Lellouch, E., et al. 2010, A&A, 521, L49
Hecht, M. H., Kounaves, S. P., Quinn, R. C., et al. 2009, Science, 325, 64
Hiesinger, H., & Head III, J. W. 2004, J. Geophys. Res.: Planets, 109, E01004
Holmes, J. A., Lewis, S. R., Patel, M. R., & Smith, M. D. 2019, Icarus, 328, 232
Hossaini, R., Chipperfield, M. P., Saiz-Lopez, A., et al. 2016, J. Geophys. Res.: Atmos., 121, 14
Huynh, H. N., & McNeill, V. F. 2020, in AGU Fall Meeting Abstracts, 2020, A238-08
Huynh, H. N., & McNeill, V. F. 2021, ACS Earth Space Chem., 5, 1896
Hynes, R. G., Mössinger, J. C., & Cox, R. A. 2001, Geophys. Res. Lett., 28, 2827
Hynes, R. G., Fernandez, M. A., & Cox, R. A. 2002, J. Geophys. Res.: Atmos., 107, 4797
Isakson, M. J., & Sitz, G. O. 1999, J. Phys. Chem. A, 103, 2044
Jia, X., Gu, W., Li, Y. J., et al. 2018, ACS Earth Space Chem., 2, 159
Keller, J. M., Boynton, W. V., Karunatillake, S., et al. 2006, J. Geophys. Res.: Planets, 111, E03S08
Kelly, J. T., & Wexler, A. S. 2005, J. Geophys. Res.: Atmos., 110, D11201
Khayat, A., Villanueva, G., Mumma, M., & Tokunaga, A. 2017, Icarus, 296, 1
Kippenberger, M., Schuster, G., Lelieveld, J., & Crowley, J. N. 2019, Atmos. Chem. Phys., 19, 11939
Kita, D., & Stedman, D. H. 1982, J. Chem. Soc., Faraday Trans. 2: Mol. Chem. Phys., 78, 1249
Knipping, E., & Dabdub, D. 2003, Environ. Sci. Technol., 37, 275
Knipping, E., Lakin, M., Foster, K., et al. 2000, Science, 288, 301
Knutsen, E. W., Villanueva, G. L., Liuzzi, G., et al. 2021, Icarus, 357, 114266
Korablev, O., Montmessin, F., & Trokhimovskiy, A. 2018, Space Sci. Rev., 214, 7
Korablev, O., Avandaele, A. C., Montmessin, F., et al. 2019, Nature, 568, 517
Korablev, O., Olsen, K. S., Trokhimovskiy, A., et al. 2021, Sci. Adv., 7, eabe4386
Kounaves, S. P., Hecht, M. H., Kapit, J., et al. 2010, J. Geophys. Res.: Planets, 115, E00E10
Kounaves, S. P., Chaniotakis, N. A., Chevrier, V. F., et al. 2014, Icarus, 232, 226
Krasnopolsky, V. A. 2005, Icarus, 178, 487
Krasnopolsky, V. A. 2012, Icarus, 217, 144
Krasnopolsky, V. A. 2022, Icarus, 374, 114807
Krasnopolsky, V. A., Bjoraker, G. L., Mumma, M. J., & Jennings, D. E. 1997, J. Geophys. Res.: Planets, 102, 6525
Krasnopolsky, V. A., Maillard, J. P., & Owen, T. C. 2004, Icarus, 172, 537
Kukui, A., Roggenbuck, J., & Schindler, R. 1997, Berichte Bunsengesellschaft Phys. Chem., 101, 281
Laskin, A., Wang, H., Robertson, W. H., et al. 2006, J. Phys. Chem. A, 110, 10619
Lefèvre, F., & Forget, F. 2009, Nature, 460, 720
Lefèvre, F., Lebonnois, S., Montmessin, F., & Forget, F. 2004, J. Geophys. Res. (Planets), 109, E07004
Lefèvre, F., Bertaux, J.-L., Clancy, R. T., et al. 2008, Nature, 454, 971
Leu, M.-T. 1988, Geophys. Res. Lett., 15, 17
Lognonné, P., Banerdt, W., Pike, W., et al. 2020, Nat. Geosci., 13, 213
Luginin, M. 2022, Aerosols from ACS during LS 255-338 of MY 34, Mendeley Data, V1
Luginin, M., Fedorova, A., Ignatiev, N., et al. 2020, J. Geophys. Res.: Planets, 125, e2020JE006419
Luginin, M., Trokhimovskiy, A., Taysum, B., et al. 2024, Icarus, 115960
Manion, J. A., Huie, R. E., Levin, R. D., et al. 2015, National Institute of Standards and Technology, Gaithersburg, Maryland, 20899-8320
Martínez, G., & Renno, N. O. 2013, Space Sci. Rev., 175, 29
Matthiä, D., Hassler, D. M., de Wet, W., et al. 2017, Life Sci. Space Res., 14, 18
McEwen, A. S., Dundas, C. M., Mattson, S. S., et al. 2014, Nat. Geosci., 7, 53
Mellor, G. L., & Yamada, T. 1982, Rev. Geophys., 20, 851
Millour, E., Forget, F., Spiga, A., et al. 2015, in Eur. Planet. Sci. Congress, EPSC2015-438
Montabone, L., Forget, F., Millour, E., et al. 2015, Icarus, 251, 65
Montabone, L., Spiga, A., Kass, D. M., et al. 2020, J. Geophys. Res.: Planets, 125, e2019JE006111
Montmessin, F., Korablev, O. I., Trokhimovskiy, A., et al. 2021, A&A, 650, A140
Moore, J. M., & Bullock, M. A. 1999, J. Geophys. Res.: Planets, 104, 21925
Mumma, M. J., Villanueva, G. L., Novak, R. E., et al. 2009, Science, 323, 1041
Navarro-González, R., Vargas, E., de La Rosa, J., Raga, A. C., & McKay, C. P. 2010, J. Geophys. Res.: Planets, 115, E12010
Nuding, D., Davis, R., Gough, R., & Tolbert, M. 2015, J. Geophys. Res.: Planets, 120, 588
Ohno, M., Utsugi, M., Mori, T., et al. 2013, Earth Planets Space, 65, e1
Ojha, L., McEwen, A., Dundas, C., et al. 2014, Icarus, 231, 365
Olsen, K. 2021, Transient HCl in the Atmosphere of Mars (University of Oxford)
Olsen, K. S., Trokhimovskiy, A., Montabone, L., et al. 2021, A&A, 647, A161
Parker, J. K., Payne, W. A., Cody, R. J., et al. 2007, J. Phys. Chem. A, 111, 1015
Patel, M. R., Sellers, G., Mason, J., et al. 2021, ESS Open Archive, essoar.10505984.1
Poncin, L., Kleinböhl, A., Kass, D. M., et al. 2022, Planet. Space Sci., 212, 105390
Primm, K., Gough, R., Wong, J., et al. 2018, J. Geophys. Res.: Planets, 123, 2076
Rieder, R., Gellert, R., Anderson, R. C., et al. 2004, Science, 306, 1746
Rieley, H., Aslin, H. D., & Haq, S. 1995, J. Chem. Soc., Faraday Trans., 91, 2349
Sander, R., Baumgaertner, A., Cabrera-Perez, D., et al. 2019, Geosci. Model Dev., 12, 1365
Seisel, S., Pashkova, A., Lian, Y., & Zellner, R. 2005, Faraday Discuss., 130, 437
Sharp, Z., Williams, J., Shearer, C., Agee, C., & McKeegan, K. 2016, Meteor. Planetary Sci., 51, 2111

Sullivan, R. C., Guazzotti, S. A., Sodeman, D. A., et al. 2007, Atmos. Environ., 41, 7166
Summers, M. E., Lieb, B. J., Chapman, E., & Yung, Y. L. 2002, Geophys. Res. Lett., 29, 24
Taysum, B. M., & Palmer, P. I. 2020, J. Geophys. Res.: Planets, 125, e2020JE006491
Thomas, N., Ehlmann, B., Meslin, P.-Y., et al. 2019, Geophys. Res. Lett., 46, 10754
Timmreck, C. 2012, Wiley Interdiscipl. Rev.: Climate Change, 3, 545
Trokhimovskiy, A., Fedorova, A. A., Olsen, K. S., et al. 2021, A&A, 651, A32
Trokhimovskiy, A., Fedorova, A. A., Korablev, O. I., et al. 2022, in Seventh International Workshop on the Mars Atmosphere: Modelling and Observations, 3521
Vago, J., Witasse, O., Svedhem, H., et al. 2015, Solar Syst. Res., 49, 518
Villanueva, G., Mumma, M., Novak, R., et al. 2013, Icarus, 223, 11
von Glasow, R. 2010, PNAS, 107, 6594
Webster, C. R., Mahaffy, P. R., Atreya, S. K., Flesch, G. J., & Farley, K. A. 2013, Science, 342, 355
Webster, C. R., Mahaffy, P. R., Atreya, S. K., & Flesch, G. 2015, AGU Fall Meeting Abstracts, P43B-2110
Webster, C. R., Mahaffy, P. R., Atreya, S. K., et al. 2018, Science, 360, 1093
Webster, C. R., Mahaffy, P. R., Pla-Garcia, J., et al. 2021, A&A, 650, A166
Wilson, E. H., Atreya, S. K., Kaiser, R. I., & Mahaffy, P. R. 2016, J. Geophys. Res. (Planets), 121, 1472
Wong, A. S., & Atreya, S. K. 2004, Adv. Space Res., 33, 2236
Wong, A.-S., Atreya, S. K., & Encrenaz, T. 2003, J. Geophys. Res.: Planets, 108, 5026
Wu, Z., Li, T., Li, J., Yang, C., & Cui, J. 2022, Remote Sens., 14, 2235
Xu, Z., & Lin, M.-C. 2003, J. Chem. Phys., 119, 8897
Zahnle, K., Freedman, R. S., & Catling, D. C. 2011, Icarus, 212, 493
Zhang, X., Berkinsky, D., Markus, C. R., et al. 2021, Icarus, 376, 114832
Zhu, R., & Lin, M.-C. 2003, J. Chem. Phys., 119, 2075
Zurek, R. W., Chicarro, A., Allen, M. A., et al. 2011, Planet. Space Sci., 59, 284

Appendix A: Alternative mechanisms for HCl production

Appendix A.1: Gas-aerosol reactions

Based on Mars Science Laboratory ChemCam analysis of bedrock from Gale Crater, Thomas et al. (2019) hypothesise that halite (NaCl) is the chloride salt responsible for producing a correlation between Na^+ and Cl^- cation measurements of bedrock. Mars Odyssey's Thermal Emission Imaging System also observed a chloride salt bearing feature whose lack of visible-to-near-infrared spectra consistent with a silicate-halite mixture of 10–25% NaCl (Glotch et al. 2016). Knipping et al. (2000) first proposed a heterogeneous mechanism that occurs on aqueous-phase NaCl dust particles on Earth, in order to help explain Cl_2 measurements and rates of organic species decay in the marine-boundary layer; this was later refined (Knipping & Dabdub 2003; Laskin et al. 2006). Hydroxyl radicals (OH) bind to solid-state NaCl in mineral dust aerosol particles to produce an OH·Cl intermediate at the surface. These intermediates react with each other to release Cl_2 to stimulate Earth marine-boundary layer chlorine chemistry. The reaction is of the form

$$OH_{(g)} + Cl^-_{(aq)} \longrightarrow OH^-_{(aq)} + 0.5Cl_{2(g)}, \tag{A.1}$$

with a change in enthalpy ΔH = -101.82 kJ mol^{-1}. Uptake coefficients for OH onto mineral dust used by Knipping & Dabdub (2003) were calculated using the Cl^- soil concentration ($[Cl^-]$):

$$\gamma_{OH} = 0.04[Cl^-]. \tag{A.2}$$

The dependence on aqueous-phase chemistry at the dust surface makes these reactions unlikely, but not impossible, in a Martian environment. Recurring surface slope lineae features have been observed by the Mars Reconnaissance Orbiter (Chevrier & Rivera-Valentin 2012; McEwen et al. 2014; Ojha et al. 2014), which have been attributed to the presence of aqueous brine solutions Martínez & Renno (2013); Edwards & Piqueux (2016) associated with salts lowering the freezing point of water below local atmospheric temperatures. The stability of these features in localised regions has been reported in laboratory experiments Moore & Bullock (1999); Altheide et al. (2009); Chevrier et al. (2020), providing a plausible way for this process to occur in localised regions of Mars's atmosphere. Various chloride bearing salts have also been observed in laboratories to be stable in the aqueous-phase under Martian atmospheric conditions Gough et al. (2014); Nuding et al. (2015). Spectral features of chlorides recorded by instruments aboard the Curiosity Rover during its transit across Gale Crater were found to have some correlation with NaCl features (Thomas et al. 2019), although this was an indirect observation.

In our study, we assumed $[Cl^-]$ to be 0.49% in Eq. (A.2), a value taken from the mean of the global distribution found by Keller et al. (2006). Using climatological MCDv6.1 profiles to drive the model at latitudes 45° north and 45° south and perihelion and aphelion conditions (71° and 251° L_S), we find that our model HCl abundances are generally below the 100 pptv detection limit for ACS/MIR (REFS). As a sensitivity study, decreasing the uptake coefficients of HCl onto $CaCO_3$ and onto water ice by three orders of magnitude fails to produce model HCl at levels detectable by ACS/MIR in the altitude range 10–40 km (1–6 ppbv) for any point in time and space. For this sensitivity experiment, we find that energetically feasible gas-phase reactions with chloride minerals in airborne dust are not capable of explaining the abundances and profile shapes of HCl on Mars.

Table A.1. Change in enthalpy (ΔH) for hydration reactions of chloride salts in Martian dust (Manion et al. 2015).

Reaction	ΔH (kJ mol^{-1})
$H_2O_{(g)} + CaCl_{2(s)} \longrightarrow CaO_{(s)} + 2HCl_{(g)}$	217.91
$2H_2O_{(g)} + CaCl_{2(s)} \longrightarrow Ca(OH)_2(s) + 2HCl_{(g)}$	108.76
$H_2O_{(g)} + NaCl_{(s)} \longrightarrow NaOH_{(s)} + HCl_{(g)}$	134.72
$H_2O_{(g)} + KCl_{(s)} \longrightarrow KOH_{(s)} + HCl_{(g)}$	161.41
$2H_2O_{(g)} + MgCl_{2(s)} \longrightarrow Mg(OH)_{2(s)} + 2HCl_{(g)}$	16.00
$2H_2O_{(g)} + FeCl_{2(s)} \longrightarrow Fe(OH)_{2(s)} + 2HCl_{(g)}$	66.83
$3H_2O_{(g)} + FeCl_{3(s)} \longrightarrow Fe(OH)_{3(s)} + 3HCl_{(g)}$	21.16

Appendix A.2: Mineral dust hydration

The correlation in observed vertical distributions of HCl and H_2O (Aoki et al. 2021; Olsen et al. 2021) is also consistent with a direct interaction between H_2O and the dust grains. However, the production of gas phase HCl purely from mineral hydration is unlikely. Chloride salts composed of the dominant cations measured at the Phoenix Lander site (Mg^{2+}, Na^{2+}, Ca^{2+}, and K^+ at 3.3, 1.4, 0.60, and 0.39 mM, respectively) are incapable of spontaneously producing gas-phase chlorine species from hydrolysis alone – Table A.1 presents the change in enthalpy from a selection of hydrolysis reactions.

Reactions with negative changes in enthalpy require additional energy to be present in the system to occur. On Mars, this energy could be provided in the form of high energy (e.g. UV) photons or ionising radiation. The thin atmosphere and a lack of a strong ozone layer (O_3) provides the Martian surface with a greater UV-B (280–315 nm) and UV-C (100–280 nm) radiation flux than on Earth. The Curiosity Rover experiences a radiation dose rate of 233 ± 12 μGy day^{-1} (Matthiä et al. 2017), roughly 17 times more than that at Earth's sea level. The release of halogenated gas-phase products from the hydration alone of chlorine-bearing minerals in Martian dust is not energetically feasible, and would require an additional source of energy such as the UV radiation flux used in the laboratory work of Zhang et al. (2021) to occur spontaneously.

Appendix B: All 1D model HCl profiles from Sect. 3.1

This section includes all 77 1D model HCl profile comparisons against ACS/MIR observations. The 1D Model is driven using three climatological scenarios, as described in subsection 2.3. We present our results on ascending order of latitude from 73.6°S to 64.9°N. The differences in latitude (Δ Lat, °), longitude (Δ Lon, °), solar longitude (Δ L_S, °), and local time (Δ Lt, hours) between the ACS TIRVIM aerosol retrieval and the ACS/MIR HCl observation are presented in each comparison plot.

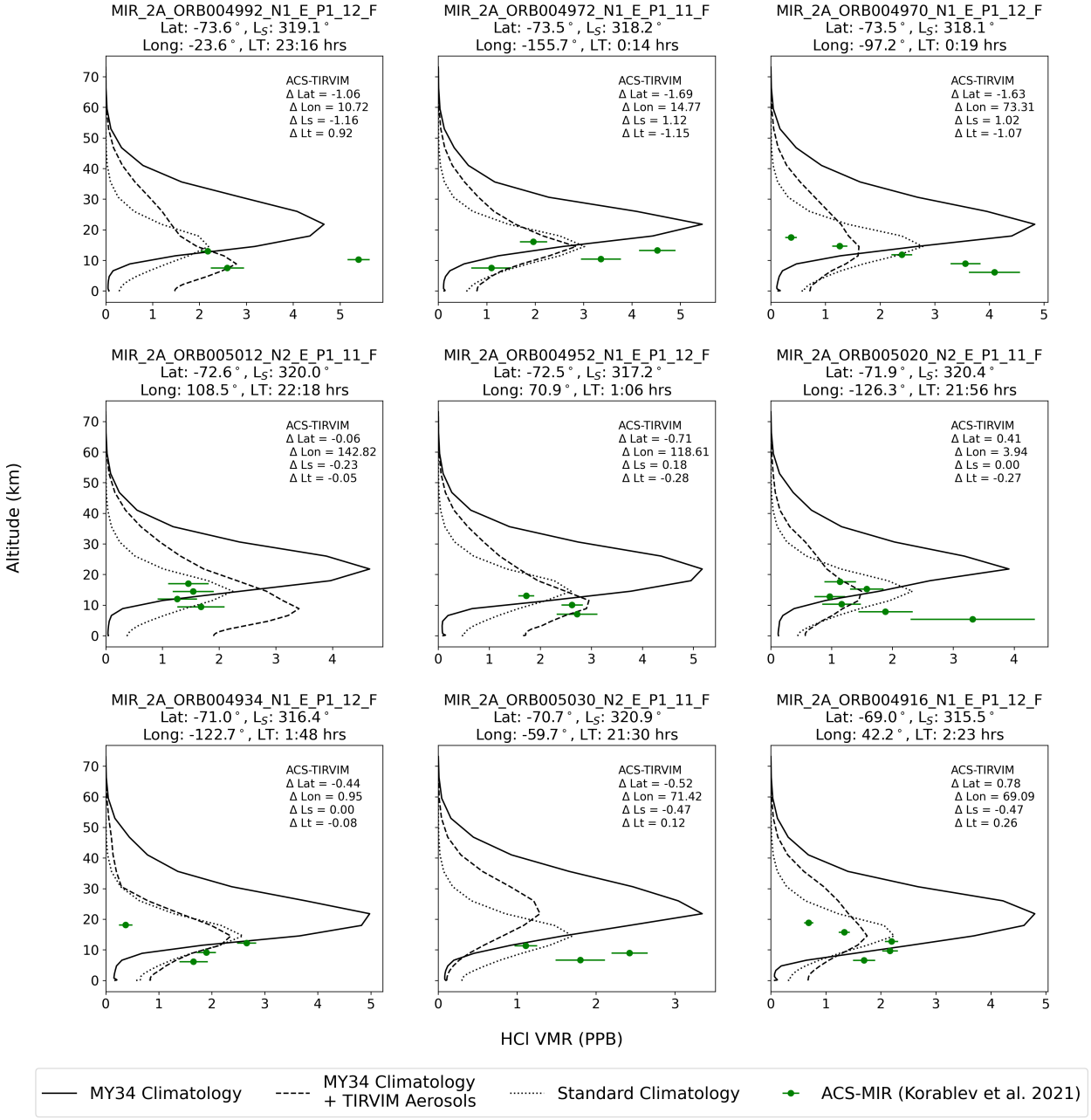

Fig. B.1. 1D HCl profile comparisons from 73.6° S – 69.0° S.

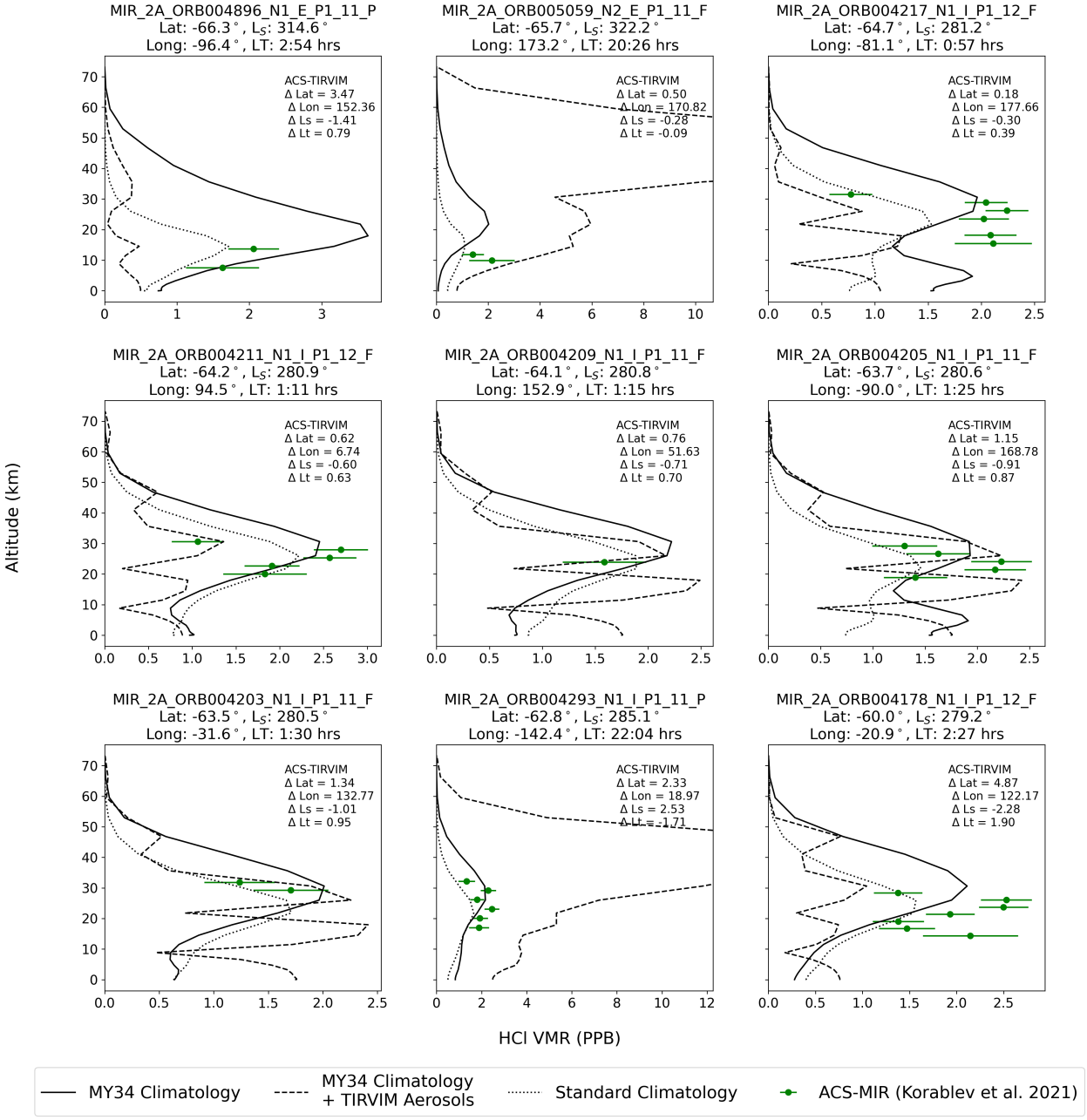

Fig. B.2. 1D HCl profile comparisons from 66.3° S – 60.0° S.

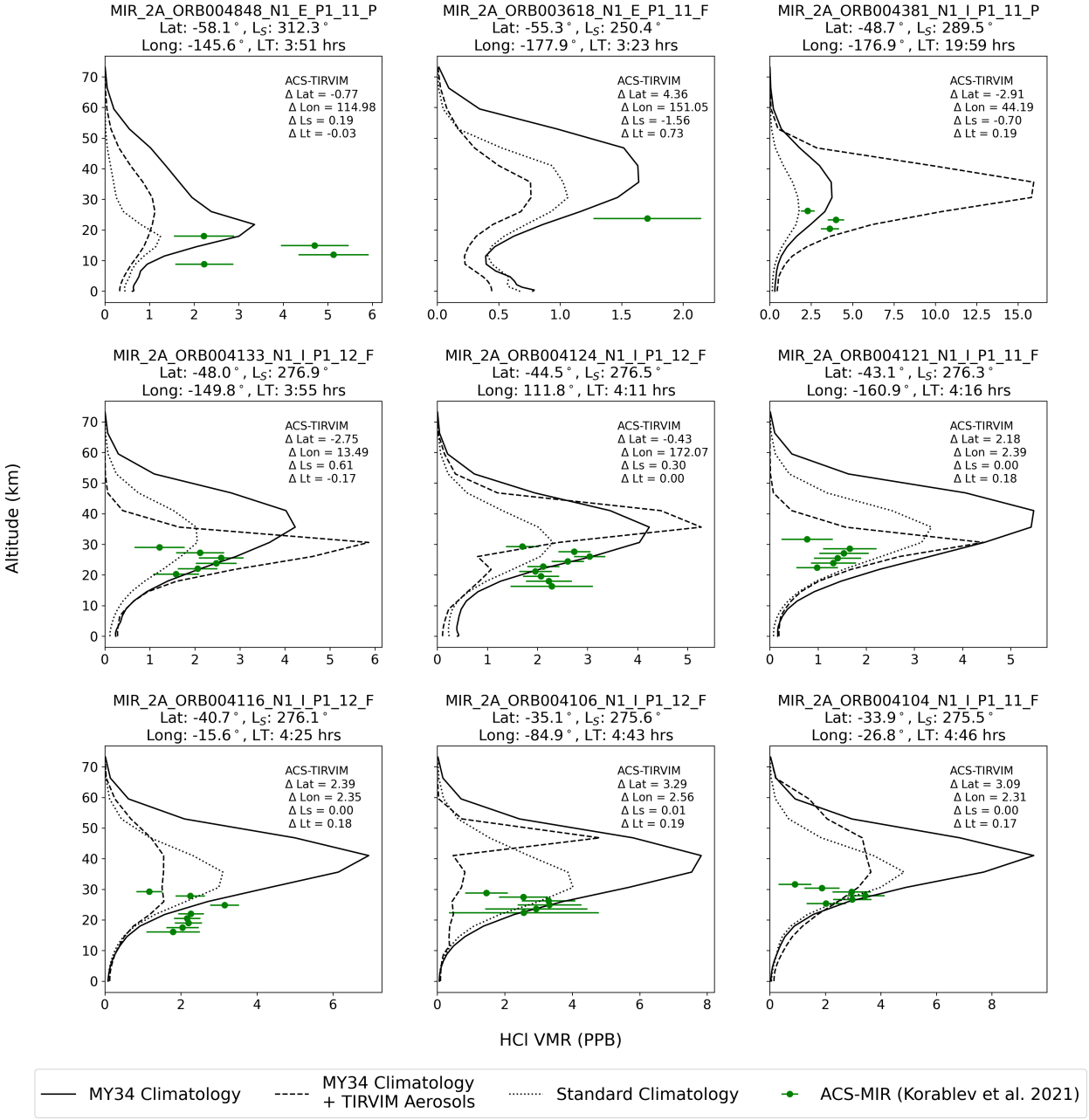

Fig. B.3. 1D HCl profile comparisons from 58.1° S – 33.9° S.

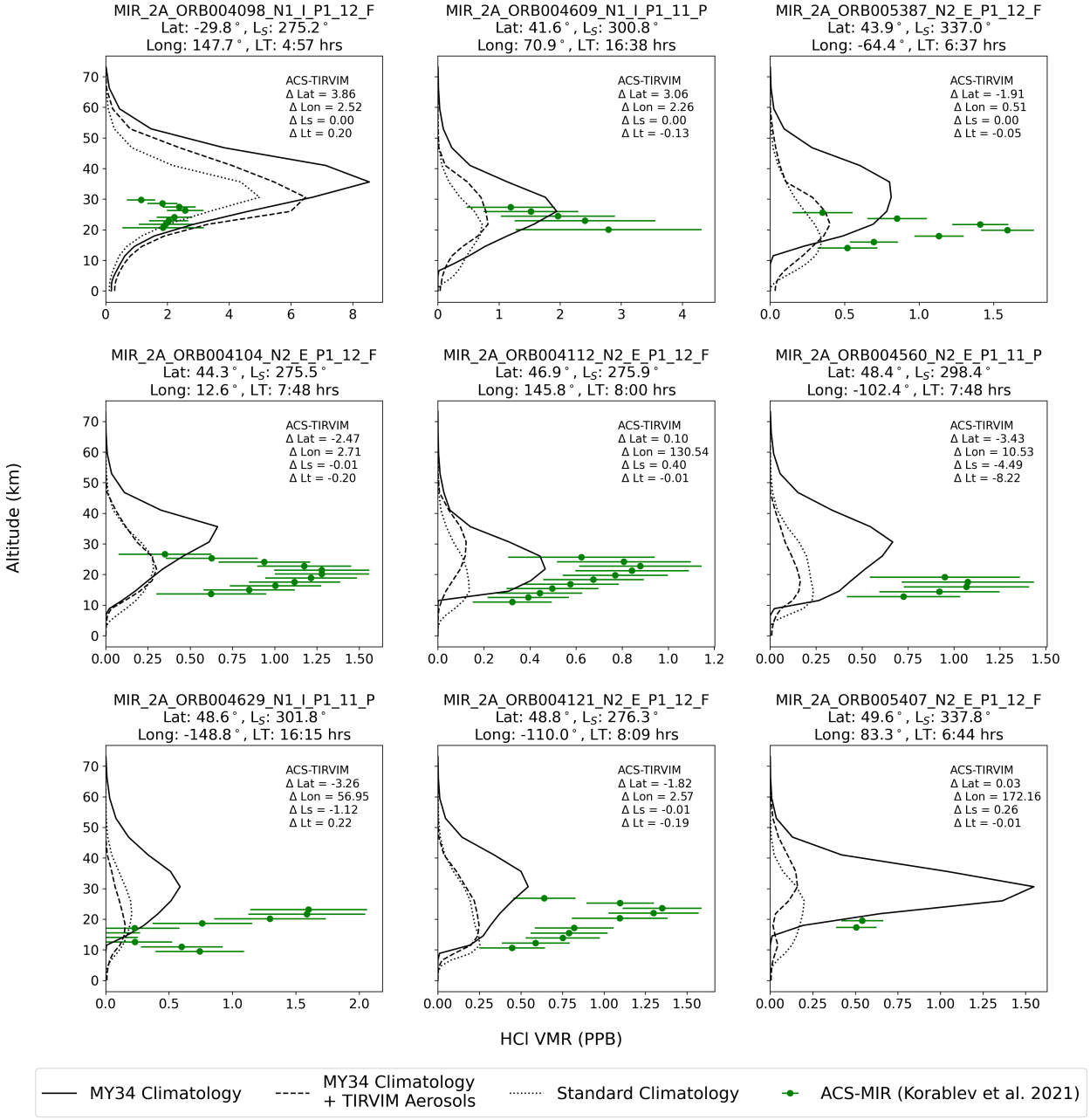

Fig. B.4. 1D HCl profile comparisons from 29.8° S – 49.6° N.

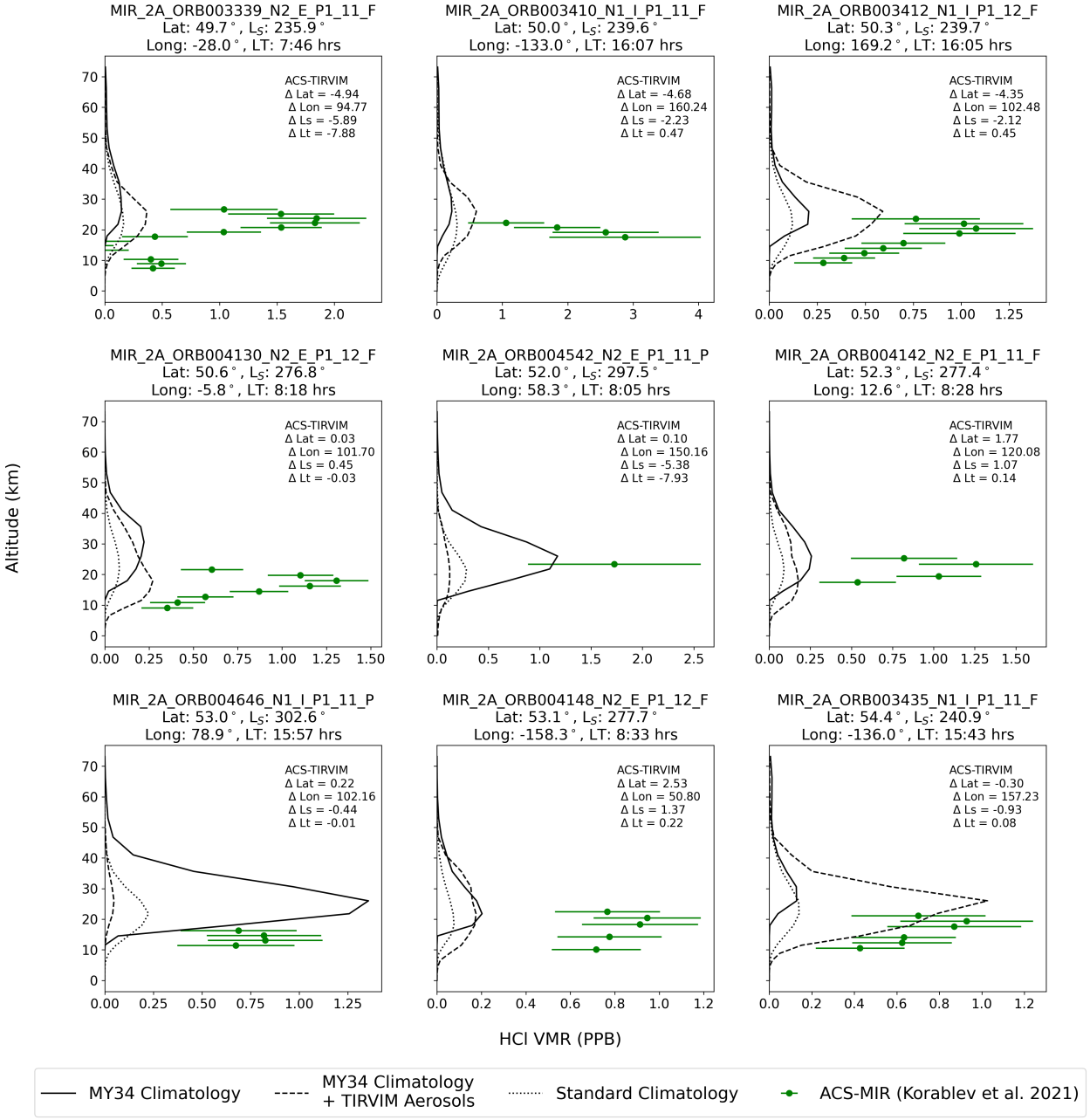

Fig. B.5. 1D HCl profile comparisons from 49.8° N – 54.4° N.

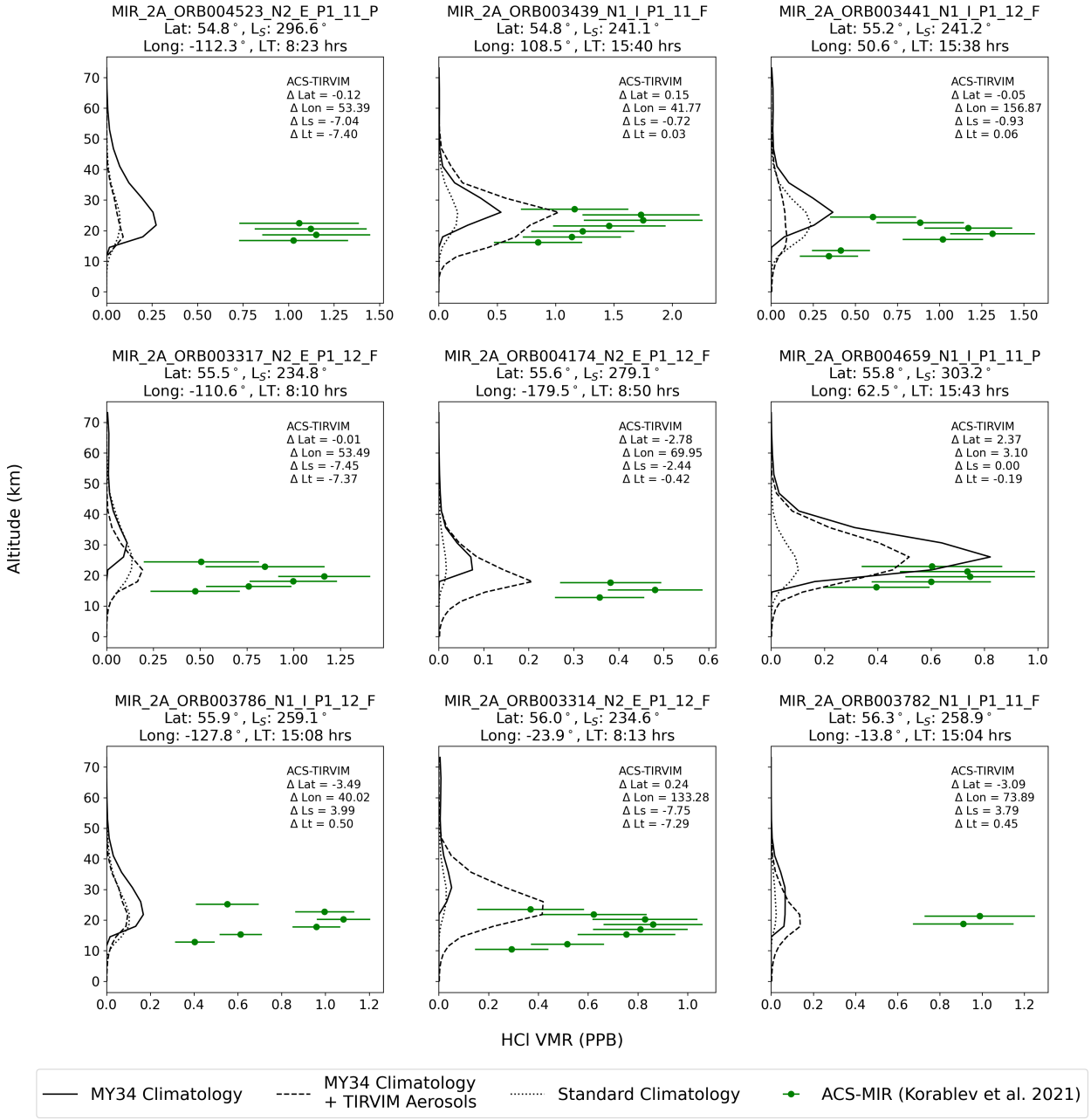

Fig. B.6. 1D HCl profile comparisons from 54.8° N – 56.3° N.

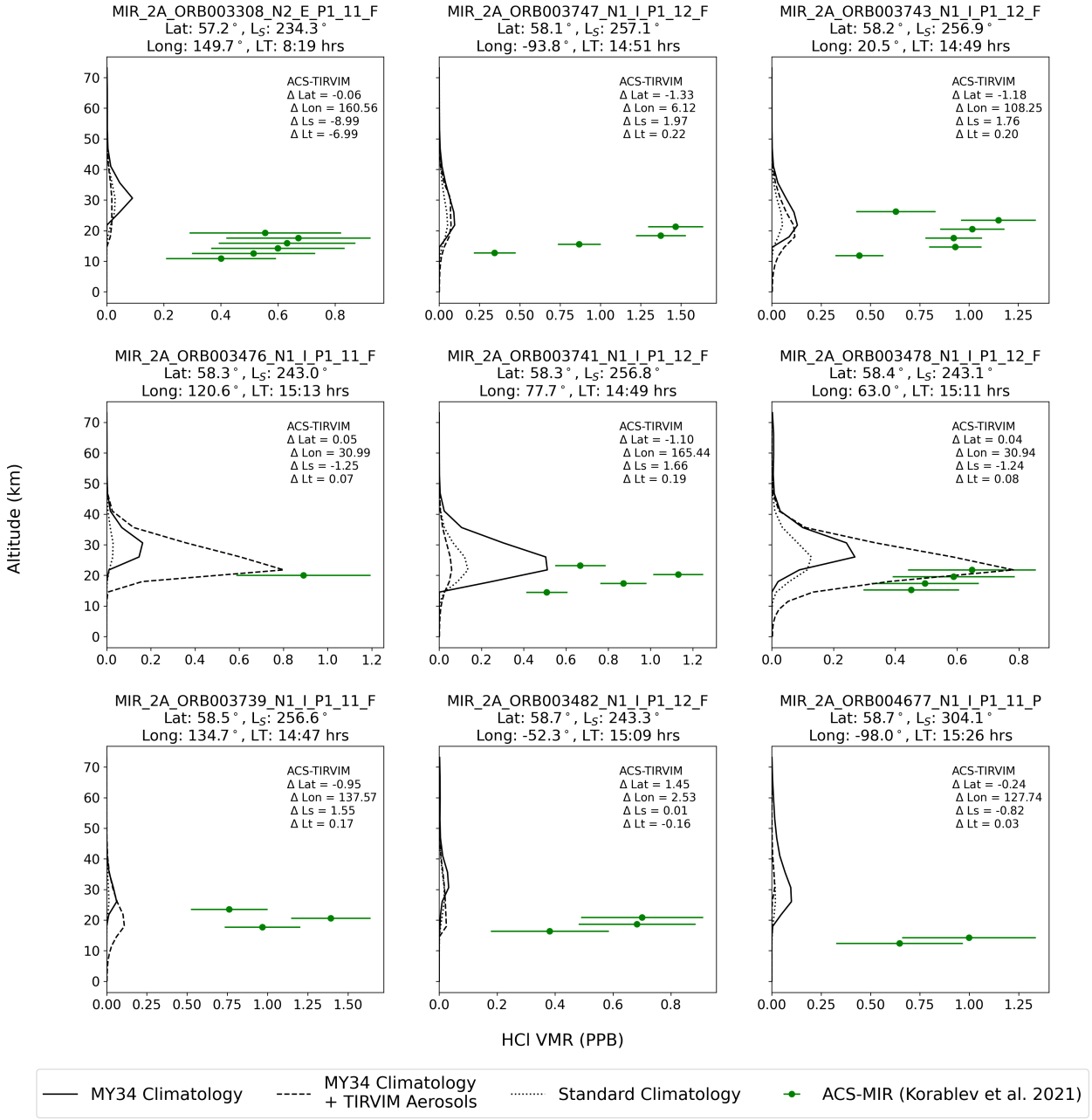

Fig. B.7. 1D HCl profile comparisons from 59.0° N – 60.8° N.

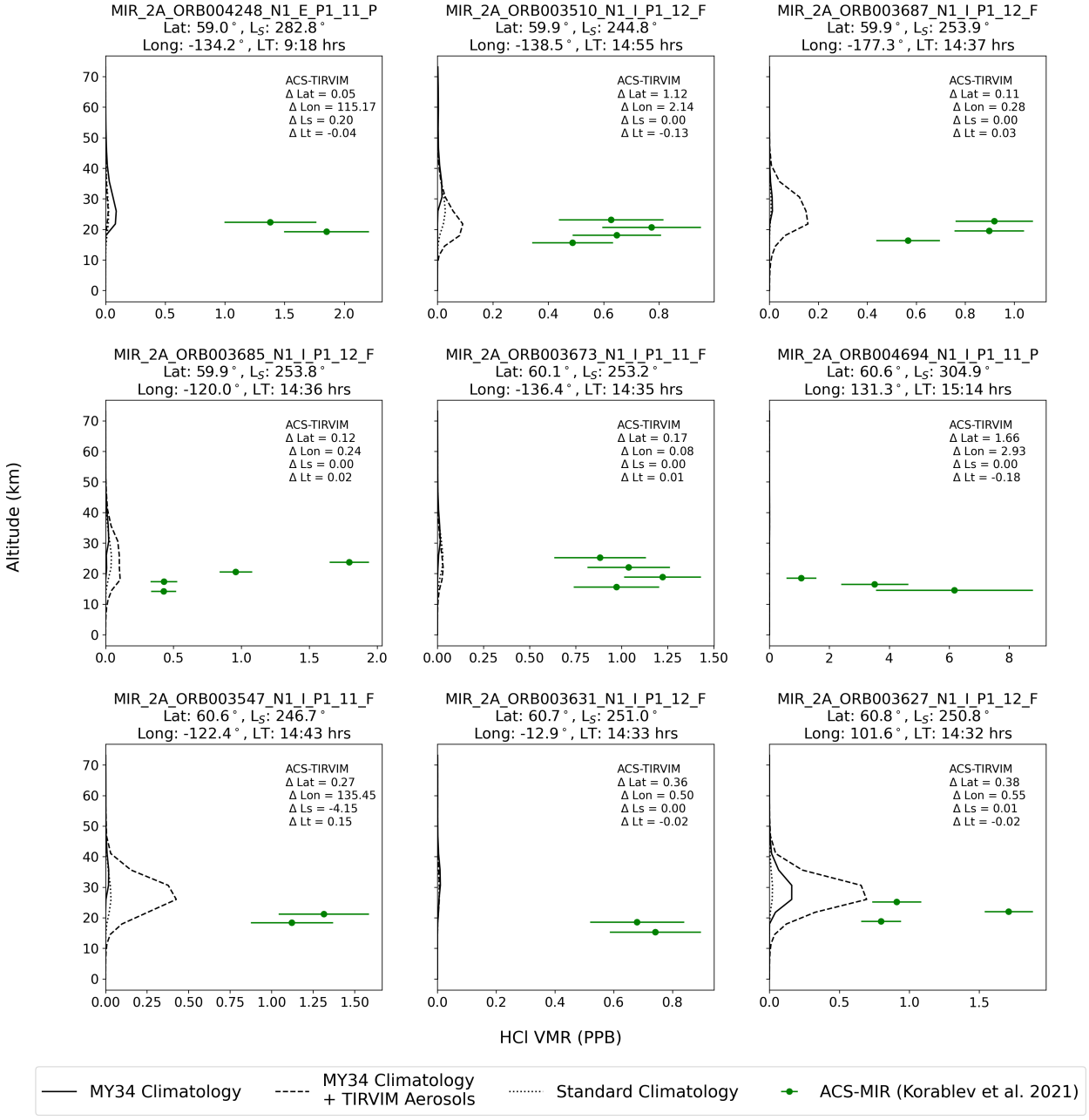

Fig. B.8. 1D HCl profile comparisons from 59.0° N – 60.8° N.

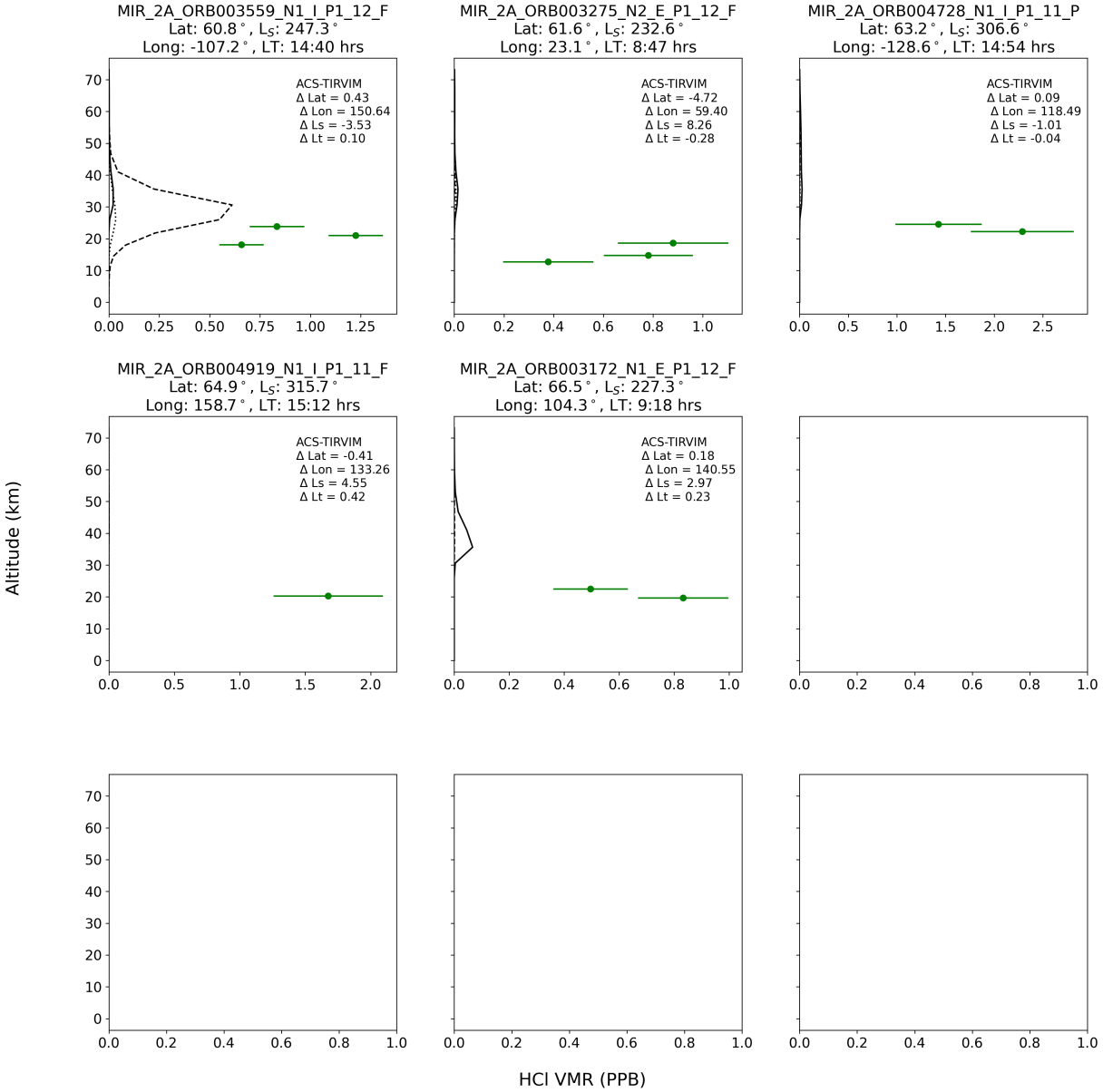

Fig. B.9. 1D HCl profile comparisons from 60.8° N – 64.9° N.

Appendix C: 1D model chemical species and rate coefficients

Table C.1. Tracer species included in the 1D photochemistry model.

Tracer Formula	Name
Inorganic Species	
CO_2	Carbon Dioxide
CO	Carbon Monoxide
$O(^1D)$	Atomic Oxygen (Excited Singlet)
$O(^3P)$ (equivalent to O)	Atomic Oxygen (Ground State)
O_2	Molecular Oxygen
O_3	Ozone
H	Atomic Hydrogen
OH	Hydroxyl
HO_2	Hydroperoxyl
H_2O_2	Hydrogen Peroxide
H_2	Molecular Hydrogen
H_2O (Vapour)	Water Vapour
N_2	Nitrogen
Ar	Argon
Aerosols	
H_2O (Ice)	Water Ice
Dust	Dust
Organic Species	
CH_4	Methane
CH_3	Methyl Radical
CH_3O_2	Methyl Peroxy-radical
CH_3OOH	Methyl Hydroperoxide
CH_3OH	Methanol
CH_3O	Methoxide
HCHO	Formaldehyde
HCOOH	Formic Acid
$HOCH_2O_2$	Hydromethyl Peroxy
$HOCH_2OH$	Methanediol
$HOCH_2OOH$	Hydromethyl Hydroperoxide
HCO	Formyl Radical
Chlorine Species	
Cl	Atomic Chlorine
ClO	Chlorine Monoxide
Cl_2	Molecular Chlorine
OClO	Chlorine Dioxide
Cl_2O_2	Chlorine Peroxide
HCl	Hydrogen Chloride
HOCl	Hypochlorous Acid
ClOO	Chloroperoxyl
CH_3OCl	Methyl Hypochlorite
CH_3Cl	Chloromethyl
ClCO	Chloroformyl Radical
ClO_3	Chlorine Trioxide
$HClO_4$	Perchloric Acid
ClO_4	Perchlorate

Appendix D: Reaction rate coefficients for chlorine photochemistry

Table D.1. Photolysis reactions of chlorine tracers used in the 1D photochemistry model.

Key	Reaction	Rate(s^{-1}) at 5.0 km	Rate (s^{-1}) at 69.5 km
j_{HCl}	$HCl + h\nu \longrightarrow H + Cl$	8.93E-8	8.22E-7
j_{HOCl}	$HOCl + h\nu \longrightarrow OH + Cl$	2.09E-4	2.80E-4
j_{ClO}	$ClO + h\nu \longrightarrow Cl + O$	2.37E-3	3.29E-3
j_{Cl_2}	$Cl_2 + h\nu \longrightarrow Cl + Cl$	2.47E-3	2.75E-3
j_{ClOO}	$ClOO + h\nu \longrightarrow ClO + O$	6.46E-3	1.36E-2
j_{OClO}	$OClO + h\nu \longrightarrow ClO + O$	9.22E-2	1.02E-1
$j_{Cl_2O_2}$	$Cl_2O_2 + h\nu \longrightarrow Cl + ClOO$	3.87E-3	6.38E-3
j_{CH_3OCl}	$CH_3OCl + h\nu \longrightarrow CH_3O + Cl$	1.12E-4	1.59E-4
j_{CH_3Cl}	$CH_3Cl + h\nu \longrightarrow 0.89CH_3 + 0.89Cl + 0.11CH_2Cl + 0.11H$	1.78E-7	7.16E-7

Rates are extracted for an atmosphere at perihelion ($L_S = 251°$) with solar zenith angle set to 60° and optical opacity at 7hPa of 0.2.

Table D.2. Heterogeneous reactions involving chemistry species studied in the 1D photochemistry model.

Key	Heterogeneous Reaction	Uptake Coefficient (γ)	Citations
h_{Cl1}	$6H_2O + h\nu + Dust_{Mg(ClO_4)_2} \longrightarrow Cl + 4O + Dust_{Mg(ClO_4)\cdot 6H_2O}$	$6.20\times10^{-2} \times$ MIN(RH,1.0) $\times j_{ClO}$	This study, motivated by Zhang et al. (2021)
h_{Cl2}	$HCl + Dust_{CaCO_3} \longrightarrow$ Products	MPM[a](0.02, 2.03E3, 12.30E3)	Huynh & McNeill (2021) and Huynh & McNeill (2020) fit to the MPM ((Berland et al. 1997))
h_{Cl3}	HCl + Ice $\longrightarrow$ Products	MPM(0.09, 8.33E8, 30.50E3) $\times$ (1 - θ_{Lang})	Hynes et al. (2001)
h_{Cl4}	$Cl_2 + Dust_{NaCl} \longrightarrow$ Products	1E-5	Burkholder et al. (2019) upper limits
h_{Cl5}	ClO + Ice $\longrightarrow$ Products	1E-4	Burkholder et al. (2019) upper limits

[a] MPM denotes the MPM function, where MPM(A, A_{Des}/A_R, ΔE) = A $\times$ (1 + $\frac{A_{Des}}{A_R} \times$ exp(-ΔE/RT))$^{-1}$. A_{Des} (s^{-1}) denotes the pre-exponential factor of the adsorbed molecule; A_R (s^{-1}) denotes the pre-exponential factor of the adsorbed molecules ionisation; Δ E (J mol^{-1}) denotes the difference in activation energies of the Arrhenius equations controlling the absorption of molecule onto the solid and the ionisation of the adsorbed molecule at the solid surface; R (J mol^{-1} K^{-1}) is the universal gas constant; T is the atmospheric temperature.

Table D.3. Reactions involving chlorine species used in the 1D photochemistry model.

Key	Reaction	Rate Coefficient	Rate at T=298 K	Reference
cl_1	$Cl + O_3 \longrightarrow ClO + O_2$	2.8E-11exp(-250/T)	1.21E-11	Sander et al. (2019)
cl_2	$ClO + O \longrightarrow Cl + O_2$	2.5E-11exp(110/T)	3.62E-11	Sander et al. (2019)
cl_3	$ClO + ClO \longrightarrow Cl_2 + O_2$	3.0E-11exp(-1590/T)	1.45E-13	Sander et al. (2019)
cl_4	$ClO + ClO \longrightarrow Cl + Cl + O_2$	3.0E-11exp(-2450/T)	8.07E-15	Sander et al. (2019)
cl_5	$ClO + ClO \longrightarrow Cl + OClO$	3.5E-13exp(-1370/T)	3.52E-15	Sander et al. (2019)
cl_6	$ClO + ClO \longrightarrow Cl_2O_2$	$2.5\times2.0E\text{-}32\ (300/T)^4$	8.24E-15	Sander et al. (2019)
cl_7	$Cl_2O_2 \longrightarrow ClO + ClO$	$cl_6/(2.16E\text{-}27exp(8537/T))$	1.38E-10	Sander et al. (2019)
cl_8	$Cl + H_2 \longrightarrow HCl + H$	3.9E-11exp(-2310/T)	1.68E-14	Sander et al. (2019)
cl_9	$Cl + HO_2 \longrightarrow HCl + O_2$	4.4e-11 - 7.5E-11exp(-620/T)	3.46E-11	Sander et al. (2019)
cl_{10}	$Cl + HO_2 \longrightarrow ClO + OH$	7.5E-11exp(-620/T)	9.37E-12	Sander et al. (2019)
cl_{11}	$Cl + H_2O_2 \longrightarrow HCl + HO_2$	1.1E-11exp(-980/T)	4.10E-13	Sander et al. (2019)
cl_{12}	$ClO + OH \longrightarrow 0.94\ Cl + 0.94\ HO_2 + 0.06\ HCl + 0.06\ O_2$	7.3E-12exp(300/T)	2.00E-11	Sander et al. (2019)
cl_{13}	$ClO + HO_2 \longrightarrow HOCl + O_2$	2.2E-12exp(340/T)	6.89E-12	Sander et al. (2019)
cl_{14}	$HCl + OH \longrightarrow Cl + H_2O$	1.7E-12exp(-230/T)	7.86E-13	Sander et al. (2019)
cl_{15}	$HOCl + OH \longrightarrow ClO + H_2O$	3.0E-12exp(-500/T)	5.60E-13	Sander et al. (2019)
cl_{16}	$Cl + CH_4 \longrightarrow HCl + CH_3$	6.6E-12exp(-1240/T)	1.03E-13	Sander et al. (2019)
cl_{17}	$Cl + HCHO \longrightarrow HCl + HCO$	8.2E-11exp(-34/T)	7.32E-11	Sander et al. (2019)
cl_{18}	$Cl + CH_3OOH \longrightarrow HCHO + HCl + OH$	5.9E-11	5.90E-11	Sander et al. (2019)
cl_{19}	$ClO + CH_3O_2 \longrightarrow CH_3O + ClOO$	4.92E-12exp(-330/T)	1.63E-12	Atkinson et al. (2001)
cl_{20}	$ClO + CH_3O_2 \longrightarrow CH_3OCl + O_2$	2.6E-13exp(260/T)	6.22E-13	Atkinson et al. (2001)
cl_{21}	$ClO + CH_3O_2 \longrightarrow CH_3O + OClO$	1.E-15	1.00E-15	Atkinson et al. (2001)
cl_{22}	$Cl + CH_3O_2 \longrightarrow 0.5\ ClO + 0.5\ CH_3O + 0.5\ HCl + 0.5\ CH_2OO$	1.6E-10	1.60E-10	Sander et al. (2019)
cl_{23}	$CO + Cl + M \longrightarrow ClCO + M$	$2.5\times1.33E\text{-}33(298/T)^{3.8}$	5.34E-16	Atkinson et al. (2007)
cl_{24}	$ClOO + Cl \longrightarrow ClO + ClO$	1.2E-11	1.20E-11	Burkholder et al. (2019)
cl_{25}	$ClOO + Cl \longrightarrow O_2 + Cl_2$	2.31E-10	2.31E-10	Burkholder et al. (2019)
cl_{26}	$ClOO \longrightarrow O_2 + Cl$	$2.8E\text{-}10exp(-1820/T)\times[M]$	$1.00E+4^a$	Atkinson et al. (2007)
cl_{27}	$HClO_4 + OH \longrightarrow ClO_4 + H_2O$	$1.24E\text{-}8exp(-1664/T)\ T^{-2.9}$	3.11E-18	Zhu & Lin (2003)
cl_{28}	$Cl + O_2 + M \longrightarrow ClOO + M$	$2.5\times1.44E\text{-}33(298/T)^{3.9}$	5.78E-16	Atkinson et al. (2007)
cl_{29}	$Cl + CH_3OCl \longrightarrow Cl_2 + CH_3O$	5.2E-11	5.20E-11	Kukui et al. (1997)
cl_{30}	$Cl + Cl_2O_2 \longrightarrow Cl_2 + ClOO$	1.E-10	1.00E-10	Atkinson et al. (2007)
cl_{31}	$Cl + CH_3OCl \longrightarrow HCl + CH_2OCl$	9.15E-12	9.15E-12	Kukui et al. (1997)
cl_{32}	$OH + CH_3OCl \longrightarrow CH_3O\ HOCl$	2.5E-12exp(-370/T)	7.22E-13	Burkholder et al. (2019)
cl_{33}	$ClCO \longrightarrow Cl + CO$	$4.1E\text{-}10exp(-2960/T)\times[M]$	$3.21E+3^a$	Atkinson et al. (2007)
cl_{34}	$Cl_2 + O(^1D) \longrightarrow O + Cl_2$	$0.25\times7.2E\text{-}10$	1.80E-10	Burkholder et al. (2019)
cl_{35}	$Cl_2 + O(^1D) \longrightarrow Cl + ClO$	$0.75\times7.2E\text{-}10$	5.40E-10	Burkholder et al. (2019)
cl_{36}	$Cl_2 + OH \longrightarrow HOCl + Cl$	2.6E-12exp(-1100/T)	6.49E-14	Burkholder et al. (2019)
cl_{37}	$Cl_2 + H \longrightarrow HCl + Cl$	8.0E-11exp(-417/T)	1.98E-11	Berho et al. (1999)
cl_{38}	$Cl_2 + CH_3 \longrightarrow CH_3Cl + Cl$	$1.67E\text{-}13exp(664/T)\times(T/298)^{2.52}$	1.55E-12	Eskola et al. (2008)
cl_{39}	$HCl + O(^1D) \longrightarrow 0.12\ O + 0.12\ HCl + 0.22\ H + 0.22\ ClO + 0.66\ Cl + 0.66\ OH$	1.5E-10	1.50E-10	Burkholder et al. (2019)
cl_{40}	$HCl + O \longrightarrow OH + Cl$	1.1E-11exp(-3300/T)	3.64E-12	Burkholder et al. (2019)

Table D.3. continued.

Key	Reaction	Rate Coefficient	Rate at T=298 K	Reference
cl_{41}	$HCl + H \longrightarrow H_2 + Cl$	2.01E-11exp(-1790/T)	4.95E-14	Kita & Stedman (1982)
cl_{42}	$HOCl + O \longrightarrow ClO + OH$	1.7E-13	1.70E-13	Sander et al. (2019)
cl_{43}	$HCOOH + Cl \longrightarrow HCl$ + Products	2.01E-13	2.01E-13	Burkholder et al. (2019)
cl_{44}	$Cl + O_3 + M \longrightarrow ClO_3 + M$	2.5E-31	4.01E-14	Catling et al. (2010)
cl_{45}	$ClO + ClO_3 \longrightarrow ClOO + OClO$	1.85E-18exp(-2417/T) $T^{2.28}$	4.08E-17	Catling et al. (2010)
cl_{46}	$ClO + ClO_3 \longrightarrow OClO + OClO$	1.42E-18exp(-2870/T) $T^{2.11}$	1.55E-17	Catling et al. (2010)
cl_{47}	$ClO + ClO_3 + M \longrightarrow Cl_2O_4 + M$	k_3rd(1.43E-1exp(-1597/T), -10.19, 1.43e-10exp(-87/T), 0.09)	1.07E-10	Catling et al. (2010)
cl_{48}	$ClO_3 + OH \longrightarrow HClO_4$	6.67E-13	6.67E-13	Catling et al. (2010)
cl_{49}	$ClO_3 + OH + M \longrightarrow HClO_4$	k_3rd(1.90E+36exp(-5542/T), -15.3, 3.20E-10exp(-25/T), 0.07)	2.94E-10	Catling et al. (2010)
cl_{50}	$ClO_3 + OH \longrightarrow OClO + HO_2$	2.1E-10exp(-18/T) $T^{0.09}$	3.31E-10	Catling et al. (2010)
cl_{51}	$OClO + O + M \longrightarrow ClO_3 + M$	k_3rd(7.25E-31, 3.1, 8.30E-12, 1)	2.34E-13	Catling et al. (2010)
cl_{52}	$OClO + O_3 \longrightarrow ClO_3 + O_2$	2.1E-12exp(-4700/T)	2.97E-19	Catling et al. (2010)
cl_{53}	$ClO_4 + Cl \longrightarrow ClO_3 + ClO$	1.98E-10exp(-49/T) $(T/298)^{0.16}$	1.68E-10	Xu & Lin (2003)
cl_{54}	$ClO_4 + HOCl \longrightarrow ClO + HClO_4$	2.57E-14exp(-1017/T) $(T/298)^{1.73}$	8.47E-16	Xu & Lin (2003)
cl_{55}	$HOCl + Cl \longrightarrow Cl_2 + OH$	3.2E-12exp(-130/T)	2.07E-12	Burkholder et al. (2019)
cl_{56}	$HOCl + Cl \longrightarrow HCl + ClO$	2.04E-13exp(-130/T)	1.32E-13	Burkholder et al. (2019)
cl_{57}	$OClO + O \longrightarrow ClO + O_2$	2.4E-12exp(-960/T)	9.58E-14	Atkinson et al. (2007)
cl_{58}	$OClO + OH \longrightarrow HOCl + O_2$	1.4E-12exp(600/T)	1.05E-11	Burkholder et al. (2019)
cl_{59}	$OClO + Cl \longrightarrow ClO + ClO$	3.4E-11exp(160/T)	5.82E-11	Burkholder et al. (2019)
cl_{60}	$Cl_2 + CH_3 \longrightarrow CH_3Cl + Cl$	1.67E-13exp(665/T)$(T/298)^{2.52}$	1.56E-12	Eskola et al. (2008)
cl_{61}	$Cl + CH_3 \longrightarrow ClCH_3$	6.00E-11	6.00E-11	Parker et al. (2007)
cl_{62}	$CH_3Cl + O(^1D) \longrightarrow 0.1O + 0.1CH_3Cl + 0.46ClO + 0.46CH_3 + 0.35Cl + 0.35ClO + 0.09H$	2.60E-10	2.60E-10	Burkholder et al. (2019)
cl_{63}	$CH_3Cl + OH \longrightarrow CH_2Cl + H_2O$	1.96E-12exp(-1200/T)	3.50E-14	Burkholder et al. (2019)
cl_{64}	$CH_3Cl + Cl \longrightarrow CH_2Cl + HCl$	2.03E-11exp(-1110/T)	4.90E-13	Burkholder et al. (2019)
cl_{65}	$ClCO + O \longrightarrow Cl + CO_2$	3.00E-11	3.00E-11	Krasnopolsky (2022)
cl_{66}	$ClCO + NO_2 \longrightarrow Cl + CO_2 + NO$	6.00E-13exp(600/T)	4.49E-12	Krasnopolsky (2022)
cl_{67}	$ClCO + O_2 + M \longrightarrow ClCO_3 + M$	exp(600/T)×5.70E-32/(1 + M/2E+18)	5.90E-14	Krasnopolsky (2022)
cl_{68}	$ClCO + Cl \longrightarrow Cl2 + CO$	1.10E-10exp(-706/T)	9.35E-12	Krasnopolsky (2022)

All rate coefficients calculated at T = 298 K are given in units of cm^3 $molec.^{-1}$ s^{-1}, with exceptions denoted with ^{a} that are first-order and in units of s^{-1}. Termolecular rate coefficients are calculated for an atmospheric temperature of 298 K and pressure of 660 Pa. [M] denotes total atmospheric number density in molecules cm^{-3}.